frontiers | Frontiers in Marine Science

TYPE Original Research
PUBLISHED 29 March 2023
DOI 10.3389/fmars.2023.1167578

EDITED BY
Wei Li,
South China Sea Institute of Oceanology (CAS), China

REVIEWED BY
Lihua Zuo,
Texas A&M University Kingsville, United States
Qing Li,
Qingdao Institute of Marine Geology (QIMG), China

*CORRESPONDENCE
Zhifeng Wan
wanzhif@mail.sysu.edu.cn
Jiujing Shang
shjj2012@126.com

SPECIALTY SECTION
This article was submitted to Marine Biogeochemistry, a section of the journal Frontiers in Marine Science

RECEIVED 16 February 2023
ACCEPTED 14 March 2023
PUBLISHED 29 March 2023

CITATION
Chen C, Wu X, Wan Z, Shang J, Huang W, Zhang W, Liang J, Xiao Z, Zhou W and Zhong L (2023) Geochemical characteristics of sediment and pore water affected by cold seeps in southern South China Sea.
Front. Mar. Sci. 10:1167578.
doi: 10.3389/fmars.2023.1167578

Geochemical characteristics of sediment and pore water affected by cold seeps in southern South China Sea

Chongmin Chen[1], Xuewan Wu[1], Zhifeng Wan[1,2]*, Jiujing Shang[3]*, Wei Huang[3], Wei Zhang[4], Jinqiang Liang[3], Zebang Xiao[1], Wei Zhou[1] and Lifeng Zhong[1]

[1]1School of Marine Sciences, Sun Yat-sen University & Southern Marine Science and Engineering Guangdong Laboratory (Zhuhai), Zhuhai, China, [2]Guangdong Provincial Key Laboratory of Marine Resources and Coastal Engineering Zhuhai, Zhuhai, China, [3]Ministry of Land and Resources (MLR) Key Laboratory of Marine Mineral Resources, Guangzhou Marine Geological Survey, Ministry of Natural Resources, Guangzhou, China, [4]Sanya Institute of South China Sea Geology, Guangzhou Marine Geological Survey, Sanya, China

Cold seep, characterized by active material circulation and methane seepage, is of great importance to reconstruct the paleo-marine environment and trace the origin of life and the occurrence of minerals. Southern South China Sea (SCS) with ample oil and gas resources is an ideal platform for cold seep study, but information and researches on cold seeps here are rather deficient. We studied the geochemical characteristics of sediment cores and pore water combined with seismic profile information in the Beikang Basin, aiming to further understand the nature of cold seeps in this area. Results show the extremely low $\delta\ ^{13}C_{DIC}$ of pore water in each core and we also found sulfate content decreases with depth, the high content of inorganic carbon (DIC) and the corresponding minimum$\delta\ ^{13}C_{DIC}$ in pore water, the kink-type depth profiles of Sr, Ba and Ni enrichment factors and Sr/Mg in the sediments of BH-CL37, the reducing sedimentary environment constrained by the features of Mo, U and REE. The extremely negative $\delta\ ^{13}C_{DIC}$ in the pore water of the sediment cores indicates strong AOM effect in cold seeps and the main biogenic origin of methane. The SO_4^{2-} depth variation trends of pore water, the high DIC content and the lowest value of $\delta\ ^{13}C_{DIC}$ can define the approximate SMTZ depth of each sediment core effectively. We thought that fluid fluxes and tectonic settings greatly influence the sedimentary environment and geochemistry, leading to the manifest regional differences in the properties and activities of cold seeps. This study of cold seep in southern SCS proves the variation of cold seep in time and space, stressing the necessity of further region-specific analysis towards different cold seeps; and the complex conditions of SCS do function well in offering multiple types of cold seeps.

KEYWORDS

geochemistry, cold seeps, sediment, pore water, southern South China Sea

1 Introduction

Cold seep commonly occurs along the continental margin, which is generated by the concentrated upward migration of dissolved hydrocarbons and/or gaseous hydrocarbons (mainly methane) (e.g. Suess, 2014; Wan et al., 2020), and functions effectively in the element circulation (Tribovillard et al., 2013; Feng D. et al., 2018; Smrzka et al., 2020). Additionally, cold seep often nurtures a unique ecosystem with a series of typical biochemical reactions (Levin, 2005; Levin and Sibuet, 2012). Cold seep is closely related to natural gas hydrate (Ingram et al., 2016; Hu et al., 2018).

Anaerobic oxidation of methane (AOM) is an important biochemical reaction in cold seep (Reeburgh, 2007; Boetius and Wenzhöfer, 2013), mainly occurring in the sulfate methane transition zone (SMTZ), carried out by a combination of anaerobic methane-oxidizing archaea and sulfate-reducing bacteria (Boetius et al., 2000; Orphan et al., 2001). AOM can generate carbonate and hydrogen sulfide and then increase the alkalinity in the surroundings, which further promotes the precipitation of some authigenic minerals, such as authigenic carbonates and pyrites etc. (Suess, 2014; Lin Q. et al., 2016; Feng D. et al., 2018). Studies on biochemistry of sediments, pore water and authigenic minerals in cold seeps can reveal the nature and history of cold seep. Sediment pore waters can offer information of modern cold seep on a short timescale of days to months (Hu et al., 2015; Feng J. et al., 2018), while sediment cores can be used as a continuous record to reconstruct the evolution of cold seep on much longer timescales (Bayon et al., 2007; Peketi et al., 2015; Li et al., 2018). In addition, authigenic minerals precipitated in cold seep sediments at a specific depth (usually SMTZ) effectively archive the formation conditions and even the dynamics of gas hydrate reservoirs (Tong et al., 2013; Bayon et al., 2015; Wang et al., 2015; Crémière et al., 2016; Liang et al., 2017).

Researches on cold seep in South China Sea (SCS) have gained increasing concern in decades and many samples such as authigenic carbonate, mussels, sediments and pore water, from more than 40 seepage in SCS have been studied so far (Feng D. et al., 2018). However, those studies mostly focused on northern SCS, which has greatly furthered the understanding of the cold seep system of northern SCS, including the fluid source and evolution etc. of cold seeps (Feng and Chen, 2015; Liang et al., 2017; Feng D. et al., 2018). In contrast, few studies have been carried out on the activities of cold seeps in southern SCS. The trough areas such as Zengmu, Wan'an, Nanwei, Nansha and Beikang in southern SCS are reported to store rich hydrocarbon gas and gas hydrate resources, and southern SCS has tectonic environment conducive to the migration of hydrocarbon-rich fluids and extensive methane outlets (Zhu et al., 2001; Wang et al., 2006; Yao, 2007; Zhang et al., 2010; Liu et al., 2011; Trung, 2012; Wei et al., 2012). In the Beikang Basin, some evidences that may indicate existence of cold seeps have been found, including some geophysical features (such as BSR) and authigenic minerals (such as authigenic pyrite) (Figure 1) (Wang et al., 2003; Su et al., 2005; Chen et al., 2009; Chen Z. et al., 2010; Liu et al., 2011). Nonetheless, till now there are only two studies focusing on the activities of cold seeps in the Beikang Basin (Yao, 2007; Li et al., 2018; Feng J. et al., 2018), their studies showed that the sulfate-methane transition zones (SMTZ) of the four sites are between 5.3 and 8.8 mbsf and the dissolved SO_4^{2-} was predominantly consumed by the anaerobic oxidation of methane (AOM) at rates between 27 and 44 mmol $m^{-2}yr^{-1}$ only by geochemical characteristics and model of porewater near our study area in the Beikang Basin(Feng J. et al., 2018). The cold seep system and its impact on the surroundings in the Beikang Basin remain vague.

In this paper, to further understand the cold seep system of southern SCS, combining the data of sediment and pore water, we studied the geochemical characteristics of pore water (concentration of Ca^{2+}, Mg^{2+}, Cl^- and SO_4^{2-}, dissolved inorganic carbon (DIC) and $\delta^{13}C_{DIC}$) and core sediments (mineralogy, total organic carbon (TOC), $\delta^{13}C_{TOC}$, $\delta^{13}C_{TIC}$, $\delta^{18}O_{TIC}$ and element contents). Moreover, the S isotope values of tubular pyrites in the sediments were analyzed to reveal the effects of cold seep activity on pyrite precipitation to a certain extent.

2 Geological settings

Located at the intersection of the Eurasian, the Pacific and the Indo-Australian plate, the South China Sea (SCS) is in complex tectonic conditions controlled by the interaction among different plates (Morley, 2012), with an average water depth of 1212 m and a total area of 350×10^4 km^2. The SCS is topographically tilted from the periphery to the center, broad in the north and south, narrow in the west and east. Diverse landscapes such as platforms, plateaus, troughs, valleys and reefs have well been developed in southern SCS.

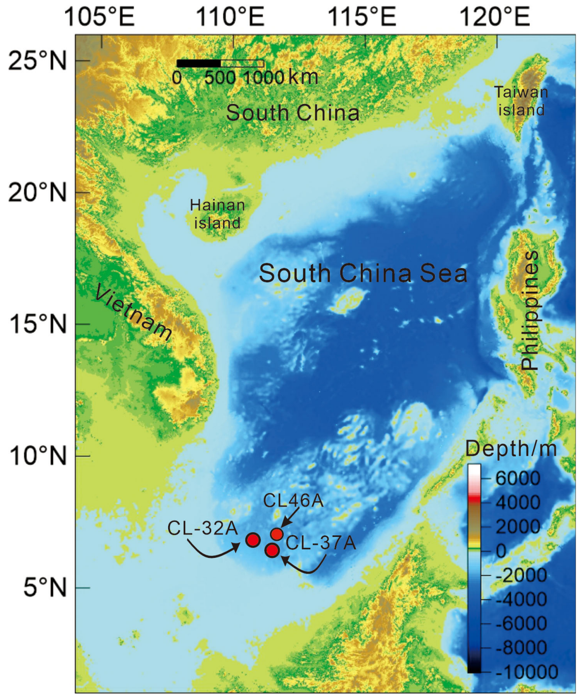

FIGURE 1
Map of the regional tectonic and sampling site locations in the Beikang basin.

The sedimentary thickness of greater than 500 m with the maximum over 10000 m, is favorable for the accumulation of sediments and the preservation of organic matter. Additionally, abundant resources of oil, gas and natural gas hydrate have been discovered in southern SCS (Fu, 2007). Gas hydrate stability zone thinned during the Last Glacial Maximum (LGM) can exhale plenty of methane, possibly promoting the formation and development of cold seeps in southern SCS (Wang et al., 2005; Yan et al., 2018).

The Beikang Basin is a Cenozoic flexural - extensional passive marginal basin in the middle of Nansha area, southern SCS (Xie et al., 2011). Its sedimentary evolution can be divided into three periods: Paleocene-Middle Eocene rift stage, Late Eocene-Middle Miocene depression stage and Late Miocene-Quaternary regional subsidence stage (Feng J. et al., 2018). Since the Palaeocene, the sedimentary environment of the Beikang Basin has gradually changed from lacustrine and littoral-neritic to a bathyal and abyssal environment (Feng J. et al., 2018). Abundant oil and gas resources have been found in the Beikang Basin. The high sedimentation rate, the deposition thickness up to 13 km and geologic structures like a large number of well-developed faults, mud diapirs and folds favoured for fluid migration, provide environment and conditions conductive to the production of oil and gas, the formation of natural gas hydrate and the migration and release of hydrocarbon (Li et al., 2018; Feng J. et al., 2018). The average value of heat flow in the Beikang Basin is 76. 8 ± 21.7 mW/m^2, which is generally higher than that of the northern SCS (Chen et al., 2017). In addition, the discovery of BSR further indicates a good potential of gas hydrate occurrences in this area.

Figures 2A, B are seismic profiles of the study area. BH-CL37 and BH-CL37A show obvious diapirs as the source of cold seep fluids, both of which are located on the same side of the fluid source, and the latter is closer to the source. There is an apparent convex phenomenon in the deep seismic profile of BH-CL37A, indicating rich fluid sources. Moreover, evident fractures, faults and other favorable fluid migration channels under the sedimentary column are present.

3 Materials and methods

The samples studied in this paper are sediment cores (BH-CL37, BH-CL37A, BH-CL32A and BH-CL46A) collected by Guangzhou Marine Geological Survey in the Beikang Basin, southern SCS, through *Haiyang IV* in 2019 (Figure 1 and Table 1). Ten cm of cores were sampled at every fifty cm, and corresponding pore water was extracted from each interval. The sediments were freezed-dried, and portions were ground to powder with an agate mortar for subsequent geochemical analysis.

3.1 Pore water

Anions (Cl^-, SO_4^{2-}) and cations (Ca^{2+}, Mg^{2+}) of pore water were measured after dilutions of 500 times with ultra-pure water by DIONEX ICS-5000 and DIONEX ICS-900 ion chromatographs respectively, with RSDs less than 3% completed at the Sun Yat-sen University Instrumental Analysis and Research Center.

In order to calculate the diffused sulfate flux, we assumed a steady-state condition and use Fick's first law (Eq. (1),(2)) for calculation:

$$J = -\varphi D_s \frac{dc}{dx} \quad (1)$$

$$D_s = \frac{D_0}{1 - ln(\varphi)^2} \quad (2)$$

Where J represents the diffusion flux of sulfate (mol m^{-2} yr $^{-1}$) and φ represents porosity (here we assume that the porosity of

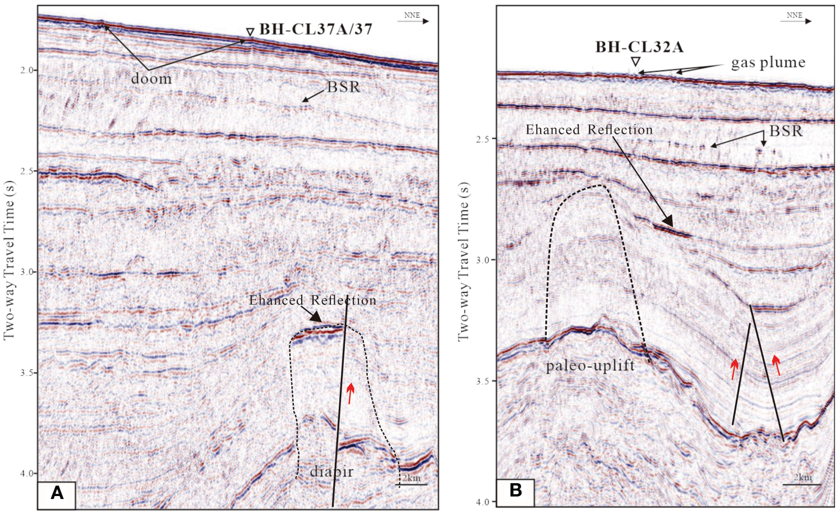

FIGURE 2
Seismic profiles of sampling sites in this study. **(A)** Seismic profile of BH-CL37, weak continuity of BSR, fault, enhanced reflection and seafloor dome; **(B)** Seismic profile of BH-CL32A, discontinuous BSR, fault, enhanced reflection and gas leakage on the seafloor.

sediments is 75%, Feng J. et al., 2018), D_0 is the diffusion coefficient of seawater ($m^2\ s^{-1}$) (Boudreau, 1997), D_S is the diffusion coefficient of sediment ($m^2\ s^{-1}$), C is the concentration of sulfate (mmol L^{-1}), X is the depth of sediment (m).

The contents of DIC and stable carbon isotopes in pore water were measured by a MAT253-Gasbench mass spectrometer in Beijing Createch Testing Technology Co., Ltd. 0.2 mL pore water was treated with pure H_3PO_4 in a glass vial of 25 °C, and the resulting CO_2 was transported by He to the mass spectrometer. The results were given in the standard δ-notation in per mil (‰) relative to the Vienna Peedee Belemnite Standard (V-PDB). $\delta^{13}C$ analysis precision is better than 0.1‰ V-PDB; The accuracy of DIC concentration analysis is better than 2%.

3.2 Sediments

The X-ray Diffraction (XRD) test of the samples was carried out at the Guangdong Provincial Key Laboratory of Marine Resources and Coastal Engineering, using a DMAX Rapid II Diffraction system (Mo Kα radiation) manufactured by Rigaku, Japan, with a working voltage of 50 kV and a current size of 30 mA. The diameter of the collimator (incident line spot) is 0.1 mm and the exposure time of each test is 10 minutes. Diffraction data were documented as two-dimensional images and then transformed into 2θ-intensity patterns by Rigaku's 2DP software.

The analyses of major and trace elements in sediments were carried out in the laboratory of Wuhan SampleSolution Analytical Technology Co., Ltd, Wuhan, China. The major elements were tested by Primus, Rigaku, Japan X-ray Fluorescence (XRF) and the Agilent 7700e ICP-MS was used for testing the trace elements. Detailed sample digestion process was described in Yang et al. (2019). The measurement precision of major elements of whole rocks is 2% and accuracy is 5%.The precision of trace element tests is 5% and the accuracy is 10%.

The total organic carbon (TOC) and $\delta^{13}C_{TOC}$ measurements were performed on an elemental analyzer manufactured by Thermoelectric Corporation of America combined with a MAT 253 plus in the laboratory of Beijing Createch Testing Technology Co., Ltd. Before TOC test, the samples were decalcified with 20% HCl for 12 h, washed with deionized water 5 times, and dried at 60 °C for 12 h. The carbon isotope analytical accuracy of the standard samples could reach 0.2 ‰ V-PDB.

Carbon and oxygen stable isotopic measurements of total inorganic carbon (TIC) in sediments were performed in the laboratory of Beijing Createch Testing Technology Co., Ltd., using the MAT253-Gas Bench Mass Spectrometer of American Thermoelectric Corporation. After the reaction of the sample and phosphoric acid, the generated CO_2 was passed through a 70 °C fused silicon capillary column for impurity separation, and finally entered into a stable gas isotope mass spectrometer for measurements. The results of carbon and oxygen isotopes are all calibrated on VPDB standard, and the analytical accuracy of both $\delta^{13}C$ and $\delta^{18}O$ is better than 0.1‰ V-PDB.

The sediment samples were sifted and dried after washing by water, and tubular pyrites were sorted out under a stereomicroscope. 200 μg pyrite was weighed with a precision balance and put into a tin cup with 3 times of the combustion-supporting agent V_2O_5. The samples were put into the automatic sampler and combustioned rapidly and fully at 1020 °C to produce SO_2 gas, which were then fed into the mass spectrometer by the He carrier gas through the splitter interface. The tests were carried out by MAT253 Plus stable isotope mass spectrometer combined with elemental analyzer (EA-IRMS). The international standard used was IAEA-S1 (Ag_2S, $\delta^{34}S$=-0.30‰ V-CDT), and the analytical deviation is better than ±0.3‰. The sulfur isotopes were normalized to $\delta^{34}S$ by Vienna Canyon Diablo Troilite (V-CDT): $\delta^{34}S$ (‰, V-CDT) = $[(^{34}S/^{32}S)_{sample}/(^{34}S/^{32}S)_{V\text{-}CDT}\ -1]*1000$.

4 Results

BH-CL37, BH-CL37A and BH-CL32A display obvious methane leakage phenomenon, while BH-CL46A does not present significant methane leakage, which is used as the reference cores for the study of pore water in this paper.

BH-CL37, BH-CL37A and BH-CL32A core sediments are mainly gray-green silty clay, fine-grained. With the increasing depth, sediments show deeper color and stronger rotten egg smell interpreted as the apparent hydrogen sulfide contents; and deep asphalt gray organic interlayers are observed at the bottom of these cores.

4.1 Pore water

4.1.1 Main cations and anions of pore water

Cl^- and Mg^{2+} in the pore water of BH-CL37, BH-CL37A, BH-CL32A and BH-CL46A generally fluctuate between 400-900 mmol/L and 28-65 mmol/L. Ca^{2+} and SO_4^{2-} in each sediment core show a decreasing trend with depth. These ions in BH-CL37 present high concentrations at the depth of 50-60 cmbsf (102.7 mmol/L Mg^{2+}, 19.3 mmol/L Ca^{2+}, 1143.3 mmol/L Cl^-, 57.6 mmol/L SO_4^{2-}) (Table 2).

In particular, Mg^{2+}/Ca^{2+} ratios of BH-CL46A, BH-CL37A and BH-CL32A vary greatly and similarly (Figure 3), while Mg^{2+}/Ca^{2+} ratios increase slowly with depth in a minor range in BH-CL37.

In BH-CL37, BH-CL37A and BH-CL32A cores, a quasi-linear decline of sulfate concentration can be observed among the depths of 350-600 cmbsf, 170-360 cmbsf and 350-540 cmbsf. Calculated sulfate fluxes of BH-CL37A and BH-CL32A are 110 mol $m^{-2}\ yr^{-1}$, 135 mol $m^{-2}\ yr^{-1}$ and 119 mol $m^{-2}\ yr^{-1}$, respectively (Figure 4).

4.1.2 DIC and $\delta^{13}C_{DIC}$ of pore water

The $\delta^{13}C_{DIC}$ values of pore water in BH-CL46A show a slight decrease trend with the increase of depth, and the variation ranges are -40.73 - -16.70‰ V-PDB, -11.8 - -55.66‰ V-PDB and -40.57 - -21.24‰ V-PDB, respectively. The $\delta^{13}C_{DIC}$ values of BH-CL37, BH-CL37A and BH-CL32A are rather stable at the top section, and then decrease to the minimum values at 530-540 cmbsf, 290- 300 cmbsf and 470-480 cmbsf, respectively. There is a good correlation between the depth profiles of DIC and $\delta^{13}C_{DIC}$ (Figure 5). DIC concentrations of the pore water in BH-CL46A show a trend of slow

TABLE 1 Details of the study sites.

Site	Water depth(m)	Core length(cmbsf)	Seafloor temperature(°C)	Geothermal gradient(°C/km)
BH-CL37	1336	660	3.23	74.80
BH-CL37A		360		
BH-CL32A	1653	730	2.73	102.00
BH-CL46A	–	730	–	–

TABLE 2 Concentration of main ions, DIC and δ^{13}C$_{DIC}$ in pore water.

Sampling sites	Interval	Mg^{2+}	Ca^{2+}	Cl^{-}	SO$_4^{2-}$	ωDIC	δ^{13}C$_{DIC}$
	(cmbsf)	(mmol/L)	(mmol/L)	(mmol/L)	(mmol/L)	(μg/mL)	(‰)
BH-CL37							
	50-60	102.74	19.28	1143.33	57.60	582.04	-11.60
	110-120	66.52	12.50	772.27	37.78	665.44	-15.17
	170-180	54.79	10.54	642.06	30.96	635.98	-16.86
	230-240	58.24	10.24	681.58	32.67	798.31	-19.39
	290-300	56.78	10.23	653.21	31.34	679.42	-18.97
	350-360	58.09	10.39	697.85	32.20	939.39	-25.24
	410-420	51.71	8.58	675.93	22.00	1452.52	-37.90
	470-480	45.06	7.11	625.00	13.86	1653.93	-42.58
	530-540	39.73	5.84	605.52	6.07	2367.02	-46.37
	590-600	36.74	4.87	581.06	1.22	2569.10	-44.96
	650-660	28.84	3.65	461.85	0.88	1955.68	-32.25
BH-CL37A							
	50-60	47.02	8.48	544.95	28.32	426.15	-11.18
	110-120	47.78	8.73	544.26	27.97	475.10	-11.98
	170-180	53.04	9.76	609.27	30.96	543.01	-12.75
	230-240	45.95	7.05	537.60	23.40	929.46	-35.17
	290-300	47.83	5.09	619.79	10.57	2597.94	-55.66
	350-360	37.86	2.72	531.31	3.51	2667.72	-40.62
BH-CL32A							
	50-60	50.10	9.46	562.54	29.12	2337.34	-6.76
	110-120	57.91	10.62	649.99	32.99	491.78	-6.74
	170-180	46.55	8.43	538.89	27.53	496.30	-6.52
	230-240	49.75	9.11	568.16	29.20	416.12	-7.67
	290-300	51.76	9.49	598.62	30.93	493.08	-9.61
	350-360	43.94	8.01	505.35	25.53	576.11	-16.12
	410-420	48.15	7.48	579.81	24.07	511.63	-39.72
	470-480	47.70	5.81	624.04	15.37	1190.63	-51.45
	530-540	32.30	2.45	479.55	2.79	2611.66	-41.98
	590-600	46.98	3.50	693.74	3.81	2419.39	-27.23

(Continued)

TABLE 2 Continued

Sampling sites	Interval	Mg^{2+}	Ca^{2+}	Cl^-	SO_4^{2-}	ωDIC	$\delta^{13}C_{DIC}$
	(cmbsf)	(mmol/L)	(mmol/L)	(mmol/L)	(mmol/L)	(μg/mL)	(‰)
	650-660	36.54	2.59	531.86	2.80	3230.28	-17.50
	710-720	33.43	2.37	485.34	2.23	2274.52	-14.72
BH-CL46A							
	50-60	74.51	13.06	892.71	39.54	1168.34	-21.24
	110-120	57.75	9.28	711.98	30.45	1301.05	-24.06
	170-180	56.50	9.46	691.92	29.06	1341.11	-25.45
	230-240	58.39	9.11	729.58	28.52	1682.77	-27.30
	290-300	48.04	7.07	595.56	21.14	1555.77	-29.95
	350-360	42.60	6.01	541.50	17.05	1636.88	-32.54
	410-420	43.30	5.46	563.68	14.69	1886.05	-34.05
	470-480	46.38	5.17	628.69	12.52	2383.49	-36.65
	530-540	44.02	3.88	617.88	7.38	2776.17	-38.97
	590-600	38.54	2.76	565.04	3.31	3007.67	-40.57
	650-660	38.32	2.94	565.44	1.57	3097.25	-38.06
	710-720	36.73	2.59	546.47	0.64	3355.97	-33.39

increase with depth (1168-3356 μg/mL), while DIC concentration profiles of BH-CL37, BH-CL37A and BH-CL32A show more complicated trend (Figure 5).

4.2 Sediments

4.2.1 XRD results of the sediments

The sediments of BH-CL37, BH-CL37A and BH-CL32A are mainly composed of quartz and clay minerals (such as illite and chlorite, etc). Some sediments at shallow intervals contain relatively abundant calcite (Figure 6).

4.2.2 Major and trace elements in the sediments

The contents of some major elements in the sediments are shown in Table 3. Al contents of BH-CL37, BH-CL37A and BH-CL32A are in the range of 7.69-10.06% (9.00% on average), 7.90-9.61% (8.80% on average), 7.85-9.95% (9.26% on average) respectively. Al is used to standardize the major elements considering the variation of carbonate contents (Tribovillard et al., 2006; Tribovillard et al., 2013). Both Ca/Al and Mg/Al in each sediment core show a trend of first decreasing and finally stabilizing, and Mn/Al ratios shallower than 400 cmbsf obviously are lower in each sediment core. Ti/Al and Si/Al ratios fluctuate in a small range of 0.043-0.053 and 2.48-3.15 respectively, showing

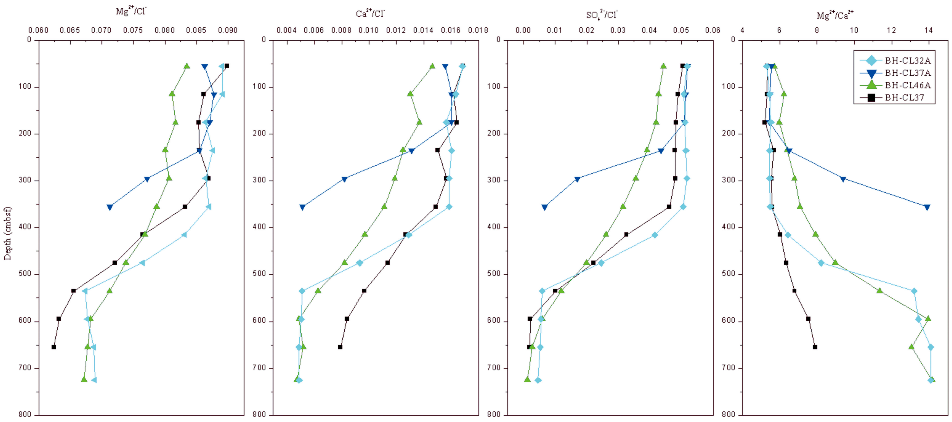

FIGURE 3
Depth profiles of Mg^{2+}/Cl^-, Ca^{2+}/Cl^-, SO_4^{2-}/Cl^- and Mg^{2+}/Ca^{2+} ratios.

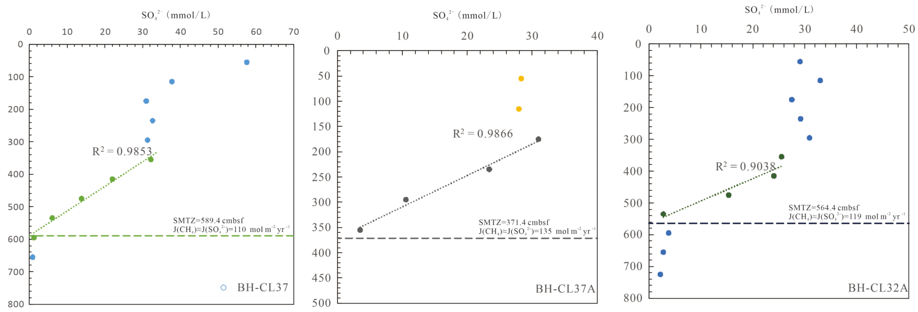

FIGURE 4
Estimated SMTZ depth and methane diffusion flux for BH-CL37, BH-CL37A and BH-CL32A cores.

relatively constant values. Fe/Al ratios have no obvious trend with depth, ranging from 0.44 to 0.52 (Figure 7).

The enrichment factor (EF) of the trace element in sediments was calculated by $X_{EF} = (X_{sample}/Al_{sample})/(X_{upper\ crust}/Al_{upper\ crust})$, where X and Al refer to the element and Al content in the sample of the upper crust (McLennan, 2001), respectively. Enrichment factor can effectively evaluate the authigenic enrichment degree of trace elements (Tribovillard et al., 2006). In general, the enrichment factor greater than 1 indicates enrichment relative to the standard (the upper crust); EF greater than 3 indicates detectable enrichment; and EF greater than 10 indicates moderate to strong enrichment (Algeo and Tribovillard, 2009).

Trace elements (Table 4) such as Mo, U, Ni, V, Co, Zn are known as redox sensitive elements and Ba content can record the activity of paleo cold seep (Dickens, 2001; Castellini et al., 2006; Riedinger et al., 2006; Joseph et al., 2013). As shown in Figure 8, except for Mo, their enrichment factors basically decrease with depth at first and then tend to be stable, and their values in the

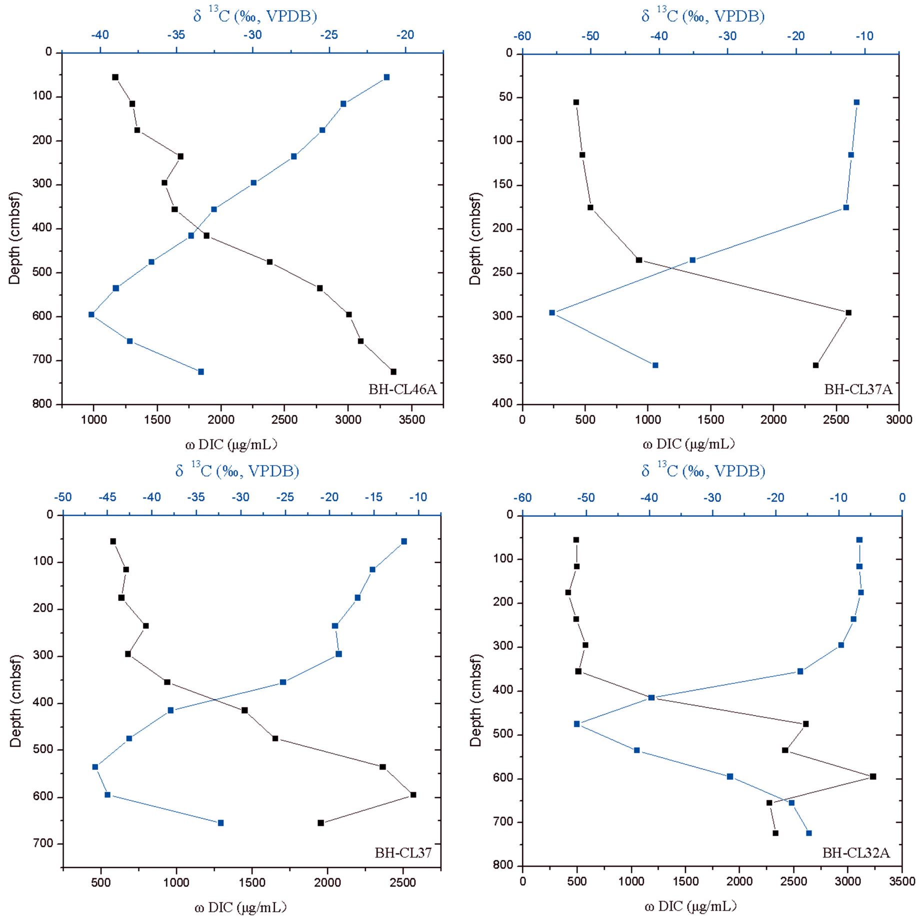

FIGURE 5
Depth profiles of DIC and $\delta^{13}C_{DIC}$ in pore water of each sediment core.

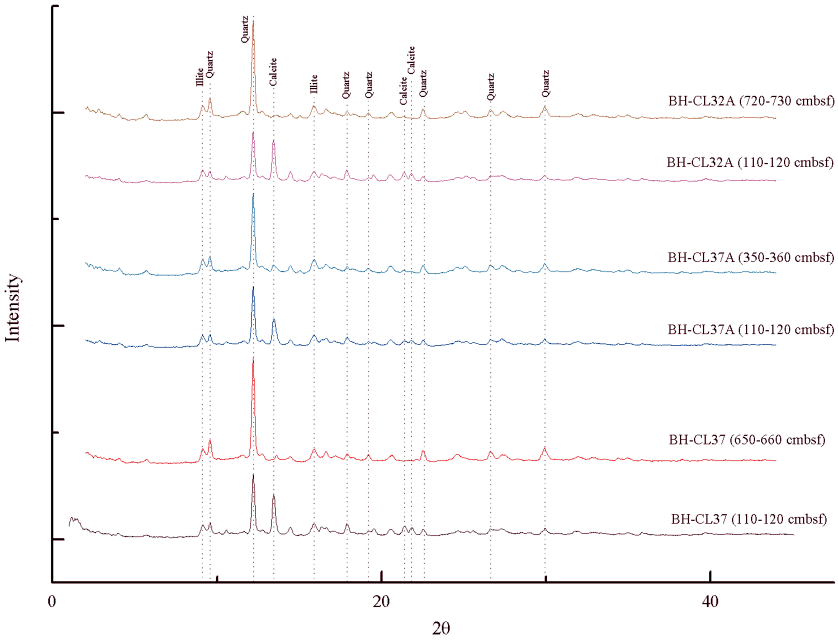

FIGURE 6
XRD results of the studied sediment cores. Shallow sediments show higher contents of calcite in each sediment core.

TABLE 3 Concentration of some major elements in sediments.

Sampling sites	Interval (cmbsf)	Al (%)	Ti (%)	Ca (%)	Mg (%)	Mn (%)	Fe (%)	Si (%)
BH-CL37								
	50-60	7.69	0.35	7.98	1.52	0.06	3.66	20.04
	110-120	7.92	0.37	7.27	1.51	0.06	4.03	20.78
	170-180	8.37	0.38	4.94	1.52	0.07	4.11	21.61
	230-240	8.88	0.39	4.17	1.46	0.05	4.33	22.72
	290-300	8.91	0.39	4.09	1.44	0.05	4.23	22.36
	350-360	9.56	0.45	1.48	1.38	0.05	4.75	25.02
	410-420	10.06	0.46	0.73	1.44	0.09	4.99	25.04
	470-480	9.28	0.47	0.56	1.31	0.08	4.57	26.91
	530-540	9.47	0.50	0.34	1.20	0.10	4.39	27.35
	590-600	9.45	0.50	0.32	1.19	0.09	4.53	27.36
	650-660	9.42	0.50	0.33	1.19	0.09	4.61	27.51
BH-CL37A								
	50-60	7.90	0.36	7.01	1.53	0.05	3.88	20.38
	110-120	8.07	0.37	6.44	1.58	0.05	3.92	21.19
	170-180	8.11	0.40	2.98	1.26	0.04	3.92	25.51
	230-240	9.53	0.43	2.30	1.44	0.05	4.53	24.25
	290-300	9.58	0.43	2.02	1.47	0.05	4.54	24.15

(Continued)

TABLE 3 Continued

Sampling sites	Interval	Al	Ti	Ca	Mg	Mn	Fe	Si
	(cmbsf)	(%)	(%)	(%)	(%)	(%)	(%)	(%)
	350-360	9.61	0.45	1.15	1.45	0.05	4.81	25.03
BH-CL32A								
	50-60	7.86	0.35	8.57	1.46	0.04	3.63	19.50
	110-120	7.96	0.36	7.63	1.48	0.04	3.81	19.98
	170-180	8.37	0.38	6.39	1.42	0.03	3.95	20.98
	230-240	9.37	0.42	2.75	1.40	0.04	4.31	23.33
	290-300	9.81	0.45	1.67	1.42	0.04	4.39	24.77
	350-360	9.76	0.47	0.58	1.30	0.05	4.78	25.78
	410-420	9.41	0.46	1.45	1.32	0.07	4.75	25.73
	470-480	9.60	0.48	0.51	1.30	0.09	4.76	26.41
	530-540	9.58	0.47	1.20	1.39	0.09	4.78	25.92
	590-600	9.95	0.48	0.42	1.40	0.09	4.77	25.64
	650-660	9.93	0.49	0.43	1.44	0.09	4.78	26.04
	710-720	9.56	0.48	0.44	1.37	0.09	4.95	26.36

shallow depths are bigger than 1. U first enriches in shallow depth, then decreases and finally tends to the equilibrium of 1 with depth in each sediment core. However, the variations of Mo enrichment factor are significantly different in the sediments: At BH-CL37, Mo_{EF} is generally less than 1, while the value as high as 12.4 suddenly appears between 350 cmbsf and 400 cmbsf; at BH-CL37A, Mo_{EF} decreases rapidly from a high value of 42.5 to a low value of about 1.4 with depth; At BH-CL32A, Mo_{EF} increases first and then decreases with depth, ranging from 0.8 to 44.8, and reaches the highest value at the depth of 410-420 cmbsf (Figure 8).

The total rare earth element (REE) contents of BH-CL37, BH-CL37A and BH-CL32A sediments range from 153.91 μg/g to 190.11 μg/g, from 151.50 μg/g to 183.24 μg/g and from 153.91 μg/g to 196.63 μg/g, respectively, generally increasing with depth (Table 5).

The studied sediments show no Eu anomaly, while most samples show no Ce anomaly, and minor show negative Ce anomaly caused by La anomaly (Figures 9 and 10).

4.2.3 TOC and $\delta^{13}C_{TOC}$ in sediments

TOC of BH-CL37 varies from 0.66% to 1.30% with an average value of 0.89%. TOC of BH-CL37A varies from 0.75% to 1.02% with an average value of 0.84%. TOC of BH-CL32A ranges from 0.69% to 1.15% with an average value of about 0.86% (Table 6).

$\delta^{13}C_{TOC}$ values of BH-CL37 greatly fluctuate at the depth of 50-420 cmbsf with a range of -23.80‰ - -21.29‰ V-PDB, and then

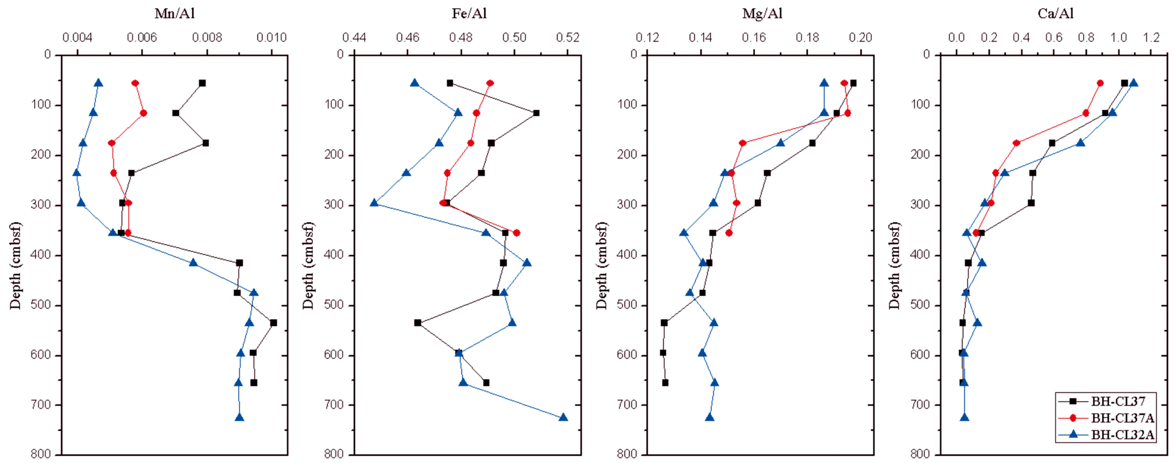

FIGURE 7
Images of the ratios of major elements to Al changing with depth.

TABLE 4 Concentration of some trace elements in sediments.

Sampling sites	Interval	Mo	U	Ni	V	Co	Zn	Ba	Cr	Cu	Sr
	(cmbsf)	(µg/g)	(µg/g)	(µg/g)	(µg/g)	(µg/g)	(µg/g)	(µg/g)	(µg/g)	(µg/g)	(µg/g)
BH-CL37											
	50-60	0.48	4.13	57.2	99.2	15.1	110	516	70.3	26.5	442
	110-120	0.70	5.06	63.9	109	17.1	118	548	76.8	29.5	419
	170-180	1.55	4.71	58.3	114	16.6	114	467	78.0	28.5	326
	230-240	1.20	5.81	51.3	114	15.6	108	478	76.8	30.4	290
	290-300	1.11	5.81	51.8	116	15.7	109	475	77.4	30.3	290
	350-360	11.1	4.28	42.6	124	16.5	104	343	80.0	21.1	142
	410-420	1.27	3.01	41.6	129	17.6	106	325	81.9	19.6	108
	470-480	0.74	3.01	36.3	118	16.0	95.2	291	77.2	17.4	94.6
	530-540	0.71	3.03	36.3	119	16.7	96.4	282	75.2	15.9	84.9
	590-600	0.68	3.09	36.5	117	16.7	96.8	283	77.2	15.9	86.9
	650-660	0.67	3.21	35.1	117	16.3	96.5	275	78.4	15.7	89.5
BH-CL37A											
	50-60	31.4	12.2	55.3	107	14.9	110	492	72.0	28.3	398
	110-120	29.7	13.6	56.2	117	15.7	111	397	77.5	28.8	366
	170-180	22.1	9.69	42.1	107	14.2	92.3	320	72.9	24.3	202
	230-240	23.4	7.67	44.0	130	17.0	103	304	80.7	21.7	160
	290-300	1.63	3.52	40.6	122	16.5	101	301	77.7	21.6	149
	350-360	1.22	3.28	40.8	126	16.7	102	309	80.4	20.5	133
BH-CL32A											
	50-60	2.43	6.44	61.2	109	15.6	124	566	74.4	31.5	483
	110-120	7.40	8.64	61.1	114	16.3	121	555	77.2	32.2	434
	170-180	15.3	8.69	56.5	120	16.2	118	517	80.0	33.4	370
	230-240	32.9	9.34	53.2	136	17.4	116	427	84.9	31.9	204
	290-300	26.0	8.94	49.9	142	17.0	116	403	88.1	29.6	151
	350-360	39.8	7.51	44.7	130	18.3	107	311	82.6	21.9	99.4
	410-420	39.4	6.32	42.9	125	17.9	100	297	81.5	20.1	112
	470-480	4.75	4.37	38.6	122	17.7	99.9	301	78.8	18.3	96.9
	530-540	1.53	3.39	38.3	118	17.2	98.0	296	76.7	18.0	122
	590-600	1.21	3.02	38.5	121	17.5	99.2	297	77.2	17.7	90.2
	650-660	0.71	3.02	38.6	126	17.5	102	294	77.9	18.3	94.8
	710-720	0.84	3.07	37.9	123	17.0	97.2	282	76.7	17.5	95.7

decrease slowly to a relatively stable value of -25.14‰ - -24.98‰ V-PDB from 530 cmbsf to 660 cmbsf with an overall mean of -23.62‰ V-PDB. $\delta^{13}C_{TOC}$ values of BH-CL37A decrease from -22.91‰ to -25.50‰ V-PDB in the depth range of 50-180 cmbsf, and then increase to -23.92‰ V-PDB with depth, finally tend to be stable gradually, with an overall mean value of -23.94‰ V-PDB. $\delta^{13}C_{TOC}$ of BH-CL32A is basically stable in the range of -22.41–21.70‰ V-PDB at the depth of 50-300cmbsf, then drops sharply to -25.88‰ V-PDB at the depth of 350-360cmbsf, and later remains relatively stable (-25.88–24.78‰ V-PDB) with an overall mean of -24.15‰ (Figure 11).

4.2.4 Carbon and oxygen isotope compositions of TIC in sediments

$\delta^{13}C_{TIC}$ values in BH-CL37, BH-CL37A and BH-CL32A are -14.15 - 0.98‰ V-PDB, -31.89 - -4.91‰ V-PDB and -29.11 - 1.26‰

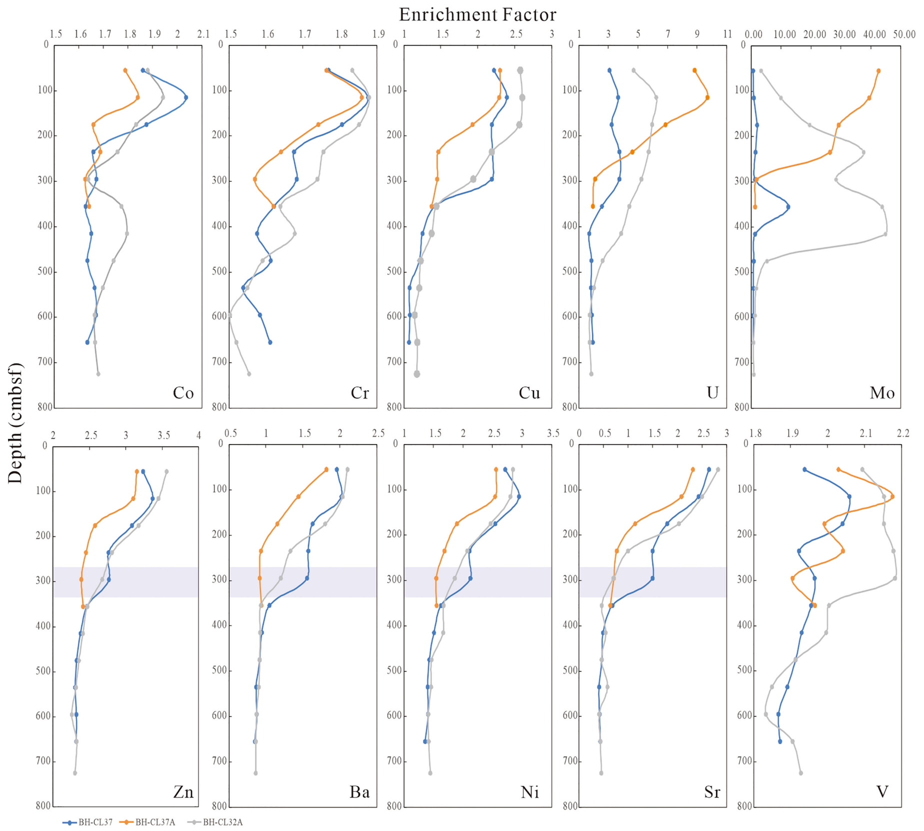

FIGURE 8
Depth profiles of trace element enrichment factors. The shadow area denotes a kink-type feature.

V-PDB, respectively, and have minimum values at 590-600 cmbsf, 230-240 cmbsf and 410-420 cmbsf. $\delta^{18}O_{TIC}$ values of BH-CL37, BH-CL37A and BH-CL32A are -2.02 - 0.15‰, -0.33 - 1.94‰ and -2.51 - 0.68‰, respectively, which are similar to the results of Li et al. (2018) (Figure 12 and Table 6).

4.2.5 Sulfur isotopes of tubular pyrites in sediments

The sulfur isotope values of pyrites in BH-CL37 sediments vary widely, ranging from -45.04‰ to 8.69‰ V-CDT. $\delta^{34}S$ fluctuates slightly at shallow depth, reaching a relatively low value at 230-240 cmbsf and 350-360 cmbsf, and a maximum value at 470-480 cmbsf. The sulfur isotopes of pyrites in BH-CL37A range from -30.58‰ to -7.81‰ V-CDT. The sulfur isotopes of pyrites in BH-CL32A vary from -27.38‰ to -15.38‰ V-CDT (Figure 13 and Table 7).

5 Discussion

5.1 AOM signals in cold seeps.

Generally, DIC in pore water in marine sediments is mainly derived from (1) DIC from overlying seawater diffusing into sediments or DIC retained during burial (usually $\delta^{13}C_{DIC}$=0 V-PDB); (2) DIC generated by degradation of organic matter; (3) DIC generated by AOM; (4) The residual DIC after methane formation (Feng D. et al., 2018; Feng J. et al., 2018). In cold seeps with active methane leakage, DIC generated by AOM often has extremely negative $\delta^{13}C$ values (usually lower than -30‰ V-PDB, Borowski et al., 2000; Claypool et al., 2006). Strong negative $\delta^{13}C_{DIC}$ values in pore water are present at the bottom of BH-CL37, BH-CL37A and BH-CL32A cores (as low as -55–35‰ V-PDB, Figure 3). In addition, considering the low content of organic matter in the sediments and the $\delta^{13}C_{TOC}$ values that vary between -25.94‰ V-PDB and -21.29‰ V-PDB (Figure 5), we infer that methane is the main source of DIC through AOM.

There are two main sources of methane in marine sediments: biogenic methane and thermogenic methane, which have different $\delta^{13}C$ characteristics. The $\delta^{13}C$ values of biogenic methane generally range from -110‰ to -50‰ V-PDB (Whiticar, 1999), while the $\delta^{13}C$ values of thermogenic methane are generally between -50‰ and -30‰ V-PDB (Sackett, 1978). Therefore, stable carbon isotopes are often used in the studies to trace the methane source in cold seeps (Feng D. et al., 2018). ^{13}C isotopes of DIC in sediment pore water can well define the source of methane (Chen Y. et al., 2010; Wang et al., 2018). Previous studies have found that the carbon fractionation between methane and DIC generated by AOM is insignificant. However, due to various mixing of different DIC sources such as seawater and organic degradation, the $\delta^{13}C$ of methane is about 10-20‰ V-PDB lighter than the $\delta^{13}C_{DIC}$ of pore water (Chen Y. et al., 2010; Feng J. et al., 2018), so the minimum value is usually used to constrain the main source of methane

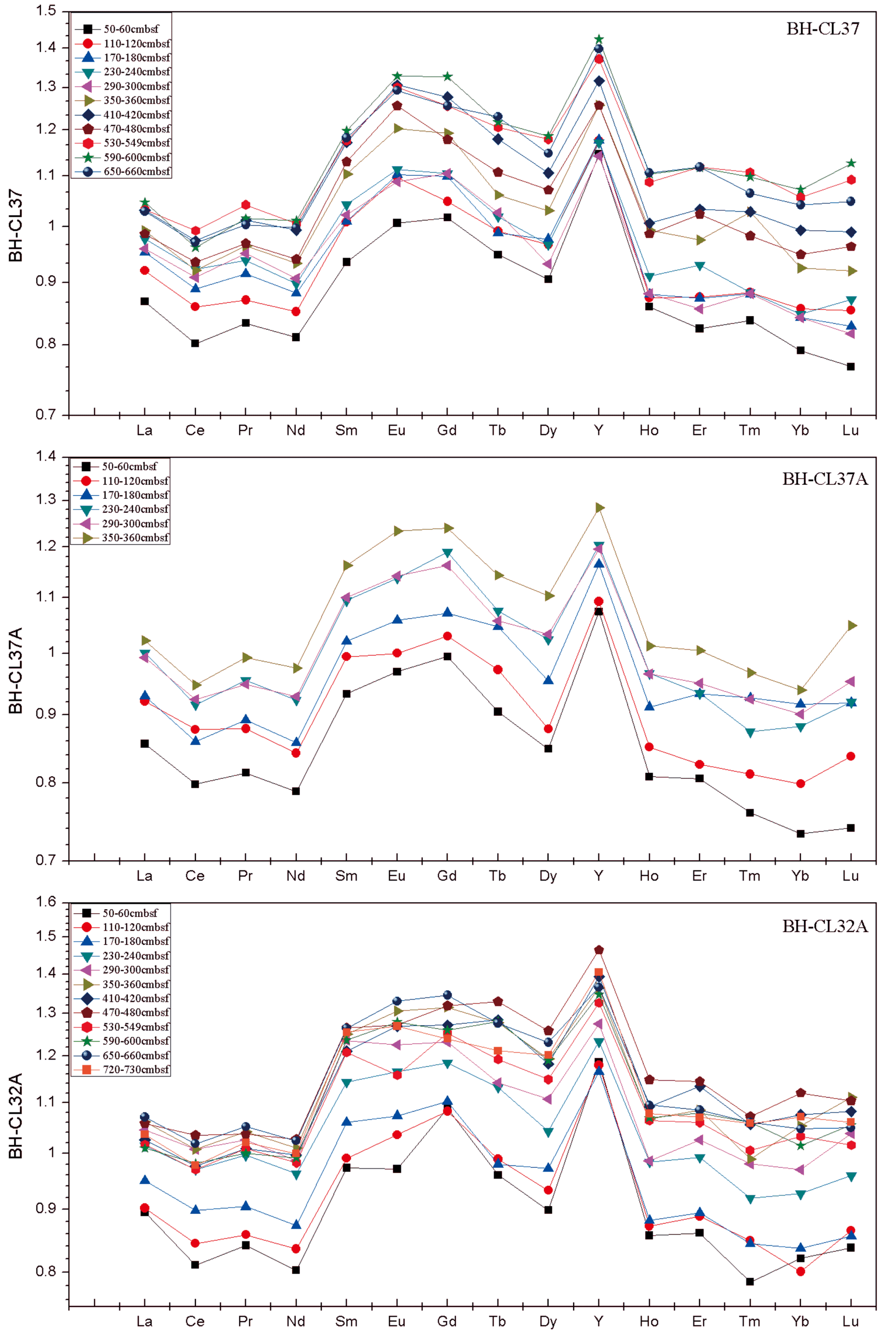

FIGURE 9
REE+Y distribution curves of BH-CL37, BH-CL37A and BH-CL32A at different depths. They are characterized as enrichment of middle rare earth element (MREE) and Y without Ce and Eu anomalies.

(Feng D. et al., 2018). The lowest $\delta^{13}C_{DIC}$ values of BH-CL37, BH-CL37A and BH-CL32A are lower than -44‰ V-PDB, indicating the microbial origin of methane in the shallow sediments of the study area. This result is consistent with that of biogenic methane obtained by Feng J. et al. (2018). Moreover, as shown in the seismic profiles of BH-CL37, BH-CL37A and BH-CL32A (Figure 2), there are obvious fluid migration channels below the sampling sites, indicating that the migration of deep fluid and thermogenic methane may play a crucial role in the sediment cores.

The sediment cores BH-CL46A show extremely negative $\delta^{13}C_{DIC}$ values as well, suggesting the abundant methane diffusion and biogenic methane. Additionally, their DIC contents increasing with depth are interpreted as the contribution of active biological reactions and methane derived from bottom (including thermogenic methane).

Based on the images of SO_4^{2-}/Cl^- (Figure 3), we infer that the approximate SMTZ depths of BH-CL37, BH-CL37A and BH-CL32A are 590-600 cmbsf, 355 cmbsf and 535-595 cmbsf,

TABLE 5 Concentration of rare earth element in sediments.

Sampling sites	Interval	La	Ce	Pr	Nd	Sm	Eu	Gd	Tb	Dy	Ho	Er	Tm	Yb	Lu	Y	TREE
	(cmbsf)	(µg/g)	(µg/g)	(µg/g)	(µg/g)	(µg/g)	(µg/g)	(µg/g)	(µg/g)	(µg/g)	(µg/g)	(µg/g)	(µg/g)	(µg/g)	(µg/g)	(µg/g)	(µg/g)
BH-CL37																	
	50-60	33.2	63.8	7.36	27.5	5.19	1.09	4.74	0.73	4.24	0.85	2.35	0.34	2.23	0.33	25.2	153.92
	110-120	35.1	68.4	7.69	28.9	5.60	1.19	4.89	0.77	4.52	0.87	2.50	0.36	2.42	0.37	25.9	163.56
	170-180	36.4	70.7	8.07	29.9	5.61	1.19	5.12	0.76	4.57	0.87	2.49	0.36	2.37	0.36	25.9	168.79
	230-240	37.3	73.4	8.29	30.4	5.78	1.20	5.15	0.79	4.52	0.90	2.65	0.36	2.39	0.38	25.8	173.60
	290-300	36.6	72.3	8.39	30.7	5.67	1.17	5.15	0.79	4.36	0.87	2.44	0.36	2.37	0.35	25.1	171.60
	350-360	37.9	73.3	8.51	31.6	6.13	1.30	5.56	0.82	4.82	0.98	2.78	0.42	2.61	0.40	27.7	177.12
	410-420	39.4	77.5	8.93	33.7	6.51	1.41	5.95	0.91	5.18	1.00	2.94	0.42	2.80	0.43	29.0	187.06
	470-480	37.7	74.4	8.55	31.9	6.27	1.36	5.49	0.86	5.01	0.98	2.92	0.40	2.68	0.42	27.6	178.88
	530-540	39.4	79.0	9.20	34.1	6.53	1.41	5.85	0.93	5.52	1.08	3.19	0.45	2.98	0.47	30.2	190.10
	590-600	40.0	76.5	8.97	34.3	6.65	1.43	6.19	0.94	5.55	1.09	3.19	0.44	3.02	0.49	31.3	188.78
	650-660	39.3	77.2	8.86	33.8	6.56	1.40	5.85	0.95	5.37	1.10	3.19	0.43	2.94	0.45	30.8	187.45
BH-CL37A																	
	50-60	32.7	63.6	7.19	26.7	5.18	1.05	4.63	0.70	3.97	0.80	2.30	0.31	2.07	0.32	23.6	151.51
	110-120	35.2	69.8	7.76	28.6	5.52	1.08	4.80	0.75	4.11	0.84	2.35	0.33	2.25	0.36	24.0	163.71
	170-180	35.5	68.4	7.87	29.1	5.66	1.14	4.99	0.81	4.46	0.90	2.66	0.38	2.58	0.40	25.6	164.86
	230-240	38.2	72.9	8.43	31.3	6.07	1.23	5.55	0.83	4.79	0.96	2.66	0.35	2.49	0.40	26.5	176.13
	290-300	37.9	73.5	8.37	31.5	6.11	1.23	5.42	0.82	4.83	0.96	2.71	0.37	2.54	0.41	26.3	176.71
	350-360	39.0	75.4	8.77	33.1	6.45	1.33	5.78	0.89	5.16	1.00	2.86	0.39	2.65	0.45	28.2	183.24
BH-CL32A																	
	50-60	34.2	64.5	7.43	27.2	5.40	1.05	5.07	0.74	4.21	0.85	2.45	0.32	2.31	0.36	26.1	156.12
	110-120	34.5	67.2	7.58	28.3	5.50	1.12	5.04	0.77	4.37	0.86	2.53	0.34	2.26	0.37	26.0	160.75
	170-180	36.3	71.5	7.99	29.6	5.88	1.16	5.14	0.76	4.55	0.87	2.55	0.34	2.36	0.37	25.6	169.34
	230-240	38.8	77.2	8.80	32.6	6.34	1.26	5.52	0.88	4.88	0.98	2.83	0.37	2.61	0.42	27.1	183.47
	290-300	39.9	80.2	9.05	33.4	6.86	1.32	5.74	0.88	5.18	0.98	2.92	0.40	2.73	0.45	28.0	190.10
	350-360	40.5	80.2	9.19	34.2	6.94	1.41	6.13	0.99	5.59	1.06	3.09	0.40	2.97	0.48	30.0	193.22

(Continued)

TABLE 5 Continued

Sampling sites	Interval (cmbsf)	La (μg/g)	Ce (μg/g)	Pr (μg/g)	Nd (μg/g)	Sm (μg/g)	Eu (μg/g)	Gd (μg/g)	Tb (μg/g)	Dy (μg/g)	Ho (μg/g)	Er (μg/g)	Tm (μg/g)	Yb (μg/g)	Lu (μg/g)	Y (μg/g)	TREE (μg/g)
	410-420	39.2	77.7	8.91	33.8	6.72	1.37	5.93	0.99	5.53	1.08	3.23	0.43	3.03	0.47	30.7	188.38
	470-480	40.4	82.4	9.15	34.8	7.02	1.37	6.14	1.03	5.89	1.14	3.26	0.43	3.16	0.48	32.2	196.63
	530-540	38.8	77.2	8.90	33.3	6.71	1.25	5.84	0.92	5.38	1.05	3.02	0.41	2.91	0.44	29.2	186.19
	590-600	38.6	78.1	8.83	33.6	6.86	1.38	5.87	0.99	5.57	1.06	3.07	0.43	2.86	0.46	29.6	187.63
	650-660	40.9	81.0	9.28	34.7	7.02	1.44	6.27	0.99	5.76	1.08	3.09	0.43	2.95	0.45	30.0	195.38
	710-720	39.6	77.8	9.02	33.9	6.97	1.37	5.78	0.94	5.63	1.07	3.05	0.43	3.02	0.46	30.9	188.99

respectively (Figure 3). Due to the intense AOM, DIC concentrations and carbon isotopic compositions of sediment pore water vary greatly in the SMTZ. The maximum DIC concentration with the corresponding minimum $\delta^{13}C_{DIC}$ value is an indicative parameter for the depth of SMTZ in cold seeps (Malinverno and Pohlman, 2011). Compared with the slow changing $\delta^{13}C_{DIC}$ values of BH-CL46A, the $\delta^{13}C_{DIC}$ depth profiles of BH-CL37, BH-CL37A and BH-CL32A all show sudden decreasing trend at a certain depth, which confirm the existence of active AOM process (Figure 5). From minimum $\delta^{13}C_{DIC}$ depth corresponding to the maximum DIC content of pore water, we infer that the SMTZ depth in each sediment core is 530-540 cmbsf for BH-CL37, 290-300 cmbsf for BH-CL37A, and 470-480 cmbsf for BH-CL32A. But for BH-CL32A site, there is a gap of 100cm between the depth of the maximum DIC concentration and the minimum $\delta^{13}C_{DIC}$ value. We think because the distance between our adjacent samples was 50cm, the accuracy was not high enough. So some key information may not be reconstructed. respectively, The depth of SMTZ is slightly shallower than the SMTZ illustrated by the minimum value of SO_4^{2-} in the depth profiles. Kim et al. (2011) explained that this deviation was related to methanogenesis reaction and other biochemical reactions in the shallow sediments. The steep reduction of Ca^{2+} and Mg^{2+} at these depths also denotes the saturation of DIC and probable precipitation of authigenic carbonates (Figure 3), confirming the strong AOM. Based on the extremely low $\delta^{13}C_{DIC}$ and positive S isotope values of the carbonates in the sediment cores, Li et al. (2018) defined the possible paleo SMTZ depths of 5.5-6.2 mbsf and 6.8-7.2 mbsf in the Beikang Basin; Feng J. et al. (2018) determined that the approximate SMTZ depth was between 5.3 mbsf and 8.8 mbsf by studying the chemical characteristics of pore water in the sediment cores in the Beikang Basin. These SMTZ depths are slightly deeper than the estimated SMTZ depths in our study area, indicating that the cold seeps studied here may have experienced more intense methane seepage activity.

In addition, considering the influence of active cold seep activity (deep fluid migration), the increase of Mg^{2+}/Ca^{2+} in the deep sediments of BH-CL37A and BH-CL32A indicates strong carbonate precipitation (Figure 3). BH-CL37, which is relatively

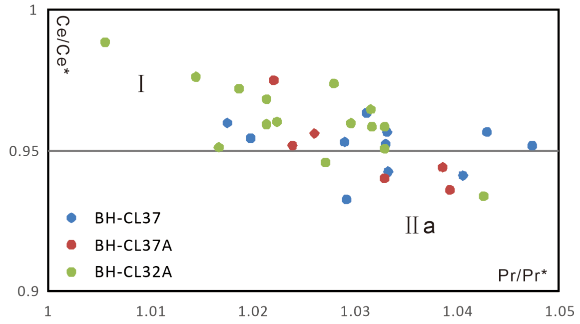

FIGURE 10
Ce/Ce* vs Pr/Pr* (Bau and Dulski, 1996; Shields and Webb, 2004) in the sediments. Zone I: no Ce and La anomaly; Zone II a: positive La anomaly, no Ce anomaly.

TABLE 6 Data of TOC, $\delta^{13}C_{TOC}$, $\delta^{13}C_{TIC}$ and $\delta^{18}O_{TIC}$ in sediments.

Sampling sites	Interval	TOC	$\delta^{13}C_{TOC}$	$\delta^{13}C_{TIC}$	$\delta^{18}O_{TIC}$
	(cmbsf)	(%)	(‰)	(‰)	(‰)
BH-CL37					
	50-60	1.09	-23.10	0.98	-0.98
	110-120	0.80	-21.95	0.25	-1.33
	170-180	1.30	-23.80	0.71	-0.52
	230-240	0.95	-21.29	0.11	-1.04
	290-300	1.16	-23.64	-0.22	-1.29
	350-360	0.86	-23.72	-1.35	-0.75
	410-420	0.69	-22.90	-3.47	-1.84
	470-480	0.80	-24.34	-6.01	-2.02
	530-540	0.78	-25.01	-13.55	0.15
	590-600	0.72	-24.93	-14.15	-1.10
	650-660	0.67	-25.14	-13.98	-0.65
BH-CL37A					
	50-60	0.79	-22.91	-4.91	-0.33
	110-120	1.01	-24.35	-17.08	0.23
	170-180	0.83	-25.50	-13.37	0.46
	230-240	0.85	-23.92	-31.89	1.94
	290-300	0.76	-23.54	-25.34	-0.20
	350-360	0.83	-23.40	-13.27	0.08
BH-CL32A					
	50-60	0.99	-22.41	1.26	-0.81
	110-120	0.72	-21.70	0.86	-0.63
	170-180	0.76	-22.13	0.16	-1.46
	230-240	0.94	-22.60	0.30	-1.39
	290-300	0.86	-22.34	0.47	-1.17
	350-360	1.14	-25.88	-0.54	-2.51
	410-420	0.76	-25.57	-29.11	0.68
	470-480	0.86	-25.61	-11.87	-2.37
	530-540	0.78	-25.94	-15.08	0.38
	590-600	1.06	-25.77	-17.20	-0.10
	650-660	0.69	-24.78	-14.01	-1.09
	710-720	0.70	-25.10	-12.99	-0.94

close to BH-CL37A, doesn't show any similar trend, which may result from too small methane flux to induce manifest carbonate precipitation (Luff and Wallmann, 2003; Karaca et al., 2010). BH-CL46A shows high value of Mg^{2+}/Ca^{2+} at the bottom, which may be affected by deep fluid environment or horizontal fluid intrusion.

Previous studies have shown steep linear sulfate gradients under high methane fluxes and strong AOM effects (Borowski et al., 1996; Borowski et al., 1999). Here, the theoretical SMTZ calculated based on the linear extension of SO_4^{2-} is approximately 589.4 cmbsf, 371.4 cmbsf and 564.4 cmbsf (Figure 4). These are very close to the depth our observed, indicating certain reliability of our calculation.

TABLE 7 Results of sulfur isotopes of tubular pyrites in sediments.

Sampling sites	Interval (cmbsf)	$\delta^{34}S$ (‰)
BH-CL37		
	230-240	-43.64
	290-300	-37.46
	350-360	-45.05
	410-420	-37.06
	470-480	8.69
BH-CL37A		
	230-240	-28.41
	350-360	-7.81
BH-CL32A		
	110-120	-22.86
	170-180	-25.32
	230-240	-27.38
	290-300	-21.21
	350-360	-15.38
	470-480	-21.12

Besides, considering that concentration of SO_4^{2-} at SMTZ is often not zero in reality, the gap between our theoretical and observed SMTZ is reasonable. Based on the 1:1 reaction relationship between SO_4^{2-} and CH_4 in the AOM reaction and the low organic matter content in the sediments of the study area, we use the change of SO_4^{2-} to roughly define the methane diffusion flux in the SMTZ of the study area, 110 mol m^{-2} yr^{-1}, 135 mol m^{-2} yr^{-1} and 119 mol m^{-2} yr^{-1}, respectively (Figure 4), higher than that calculated in Feng J. et al. (2018), which indicates the active CH_4 leakage in the study and good gas storage potential in the Beikang Basin.

In contrast to pore water, sediment cores are formed in cumulative processes that record both current and past biochemical processes in geochemical features. In this study, $\delta^{13}C_{TIC}$ values of the sediments represent the mixture of biogenic carbonates (benthic and planktic foraminiferal shells) ($\delta^{13}C_{TIC}$ of about 1.1 ‰ V-PDB) and authigenic carbonates ($\delta^{13}C_{TIC}$ smaller than -30 ‰ V-PDB) (Figure 12) (Li et al., 2018; Wang et al., 2018). Our results show the lowest $\delta^{13}C_{TIC}$ value of the sediments near the SMTZ, which indicates that the authigenic carbonates were generated by strong AOM at SMTZ.

5.2 Response of environmental geochemical characteristics to cold seep activity

5.2.1 Sulfur isotope characteristics of tubular pyrites under the influence of AOM

Previous studies have shown that the AOM process can affect both the abundance of solid sulfide phase and its sulfur isotopic compositions in sediments (Canfield and Thamdrup, 1994; Borowski et al., 2013; Lin Z. et al., 2016). Sulfate reduction in anoxic marine sediments mainly includes organoclastic sulfate reduction (OSR; Berner, 1980), and anaerobic oxidation of

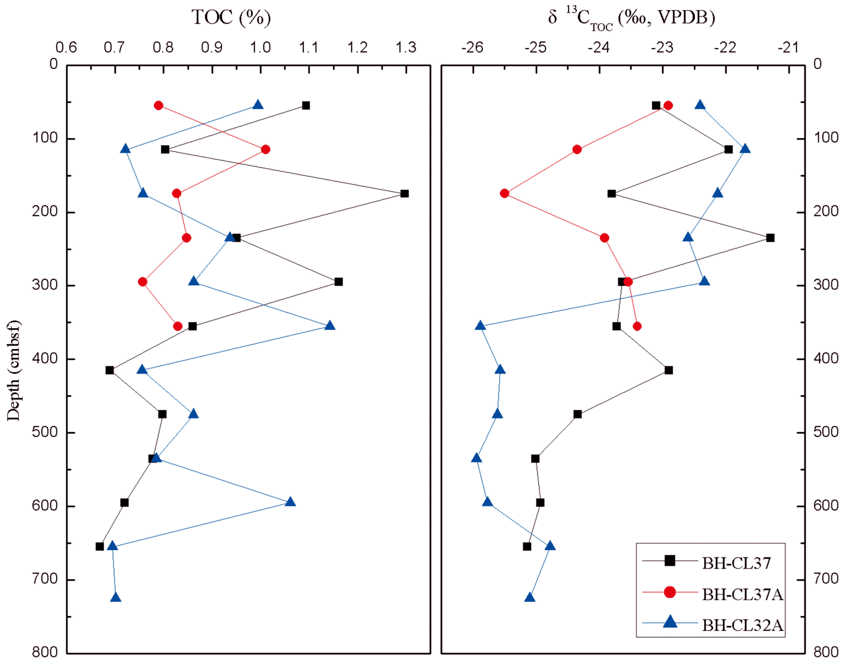

FIGURE 11
Depth profiles of TOC and $\delta^{13}C_{TOC}$ in the sediments.

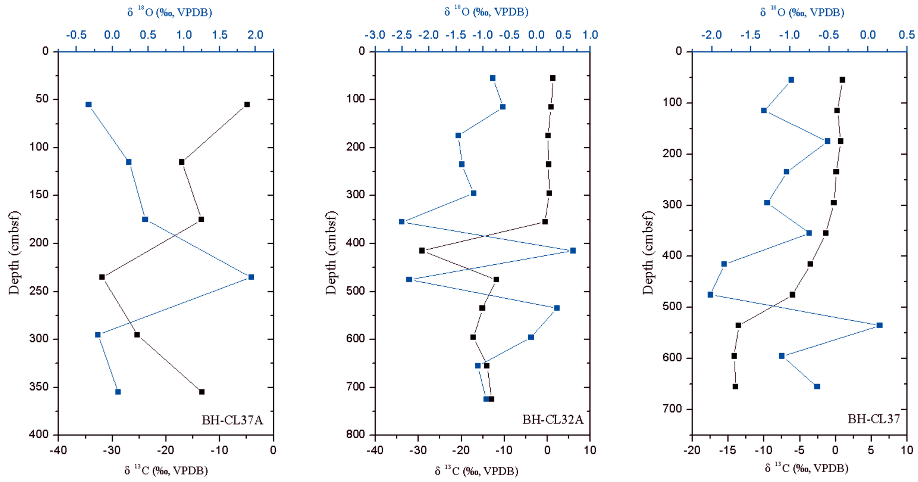

FIGURE 12
Depth profiles of the $\delta^{18}O_{TIC}$ and $\delta^{13}C_{TIC}$ in the sediments. Oxygen isotopes are shown in blue and carbon isotopes in black.

methane (AOM). The $\delta^{34}S$ value of dissolved sulfate in seawater is about 21‰ V-CDT (Rees et al., 1978), while the isotope fractionation can be as high as 60‰ V-CDT due to microbial sulfate reduction (Jørgensen et al., 2004). OSR is the main sulfate reduction process in methane-free sediments, usually leading to the production of poor ^{34}S sulfide, while ^{34}S of pyrite in methane-free sediments is often close to -50‰ to -40‰ V-CDT (Feng D. et al., 2018). In cold seeps, AOM strongly consumes sulfate under closed or semi-closed conditions, which may lead to the generation of sulfur compounds enriched in ^{34}S (Jørgensen et al., 2004; Lin et al., 2017; Feng D. et al., 2018). Although both OSR and AOM will lead to positive $\delta^{34}S$ (Feng D. et al., 2018), we think that changes of $\delta^{34}S$ at different depths at the same site can reflect the AOM process to small extent. The ^{34}S of tubular pyrites in BH-CL37, BH-CL37A and BH-CL32A have a large variation range,and present low and stable values in the shallow part, where the sulfate reduction rate is low and the fractionation is relatively thorough (Figure 13). Deeper than 350 cmbsf, all three sediment cores show high sulfur isotope values, and the values of BH-CL37A and BH-CL32A are generally bigger than -25‰ V-CDT. Both OSR and AOM will lead to positive $\delta^{34}S$, we think different ranges in sites between BH-CL37 and BH-CL32A are most likely due to the large differences in OSR rates among different sites. The values of $\delta^{34}S$ of pyrites at the bottom of BH-CL37 are even greater than 0 V-CDT, indicating that the reduction rate of sulfate is increasing. These prove the important influence of AOM on the S cycle in cold seeps, and the higher methane flux in the deeper formation also supports the AOM process. According to our results, the ^{34}S variations with depth and previous studies (Lin Z. et al., 2016; Feng D. et al., 2018), we speculate that pyrites formed near the SMTZ in the sediment core are likely to have higher ^{34}S isotope values. In addition, BH-CL37 and BH-CL37A are located at similar locations but affected by different intensities of cold seep activities, while the S isotopes of BH-CL37A are heavier in the same depth range, which may indicate a quicker sulfate consumption rate here and a stronger effect of cold seep.

5.2.2 Geochemical evidence of methane seepage variation

Cold seeps rich in methane usually have high biological abundance (Gibson et al., 2005; Campbell, 2006; Levin and Sibuet, 2012). The shallow parts of the sediment cores are abundant in the biological shells e.g. foraminifera and show a high content of Ca (Figure 7). The XRD results show that shallow sediments contain a high content of carbonates (Figure 6), mainly low magnesium calcite, which is associated with calcareous biological shells and deep fluids with low salinity.

Sr/Ca and Mg/Ca ratios in sediments have recently been used to reconstruct cold seep activities in the past in methane seepage (Yang et al., 2014; Gong et al., 2018). The images of Sr/Ca vs Mg/Ca (Figure 14) show the major calcite content with minor aragonite, which is consistent with our XRD results (Figure 6). As the depth

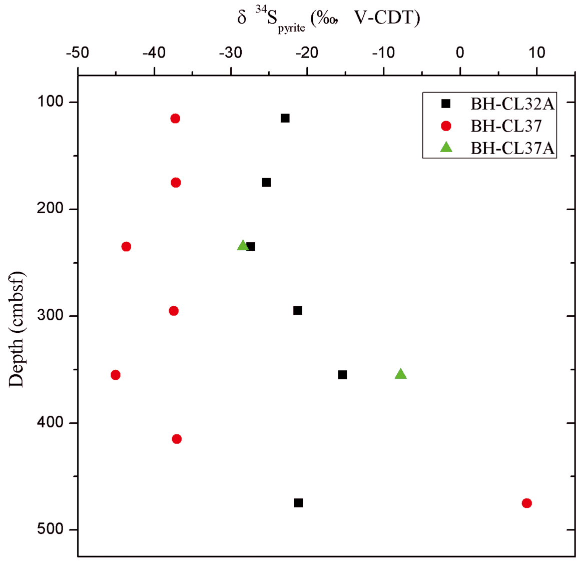

FIGURE 13
Depth profiles of sulfur isotopes of tubular pyrite in the sediment cores.

increases, the data points get closer to the reference detrital value, and there is a good correlation between Sr/Ca and Mg/Ca in the sediment cores, indicating that the influence of debris gradually increases with the increase of depth. Meanwhile, from the $\delta^{13}C_{TIC}$ and XRD results of shallow sediments, we conclude that the contents of carbonates in the sediment cores are not high enough and the carbonates in shallow sediments are mainly calcareous biological shells, which may conceal the information of authigenic carbonates. Therefore, it is difficult for Mg/Ca and Sr/Ca to directly and effectively reflect the types and formation of authigenic carbonates.

Specially, Sr, Ca/Al, Ca/Sr, Sr/Mg and Ca/Mg in the BH-CL37 sediments show a kick-type feature at depths of 290-300 cmbsf. The image of Ca^{2+}/Cl^{-} concentration in BH-CL37 pore water shows no addition of fluid from horizontal or other directions is found in this layer, and a relatively consistent Ca deposit rate is found in the corresponding depth range (Figure 3). As mentioned above, the information of elements of authigenic carbonates is easily covered by the biological shell information in the sediments, so the kick-type feature here reflects the precipitation of the authigenic carbonates with higher Ca/Sr, Sr/Mg and Ca/Mg ratios. Similar feature is also present in the depth profiles of Ba and Ni enrichment factors. Sr_{EF}, Ca concentration, Ca/Sr and Sr/Mg have a good correlation with the enrichment factors of trace elements Ba, Ni, Cu and Zn (as shown in Figure 15, Ca concentration, Ca/Sr and Sr/Mg etc. have similar relationship with these trace elements). Many studies have shown that the authigenic minerals in cold seeps may have recorded the changes of paleo cold seeps, while the Ba peak and authigenic carbonates are often considered as the indicator of paleo SMTZ (Torres et al., 1996; Dickens, 2001; Snyder et al., 2007; Vanneste et al., 2013; Gong et al., 2018; Feng D. et al., 2018). The correlations between Ni, Cu, Zn and Sr, Ca, Mg indicate that cold seep authigenic carbonates have strong enrichment and retention potential of trace elements (Smrzka et al., 2019; Smrzka et al., 2020). The good correlation between Ni and Sr is also present in our carbonate samples from southern SCS. Thus, this kick-type feature in BH-CL37 probably reflects a periodic strengthened AOM reaction, indicating the depth of the paleo SMTZ. $\delta^{34}S$ of pyrite in BH-CL37 also appears a relatively high value near the depth of 300 cmbsf, which provides evidence for the existence of paleo SMTZ.

SMTZ depth is reported to be affected by different methane fluxes (Michaelis et al., 2002; Luff et al., 2004). Generally, while the cold seep is more active, the methane flux is greater, and its SMTZ depth is shallower, and vice versa. The paleo SMTZ depth of BH-CL37 is obviously shallower than the present SMTZ depth, indicating that the methane flux of BH-CL37 was reduced and reflecting the existence of stronger methane leakage in a certain period in the past; this may be caused by the weakening of cold seep activity or the periodic decomposition of natural gas hydrate in the past, resulting in the local increase of methane. Similar feature in BH-CL37A is absent though these two cores are located closely. The reason may be that the larger and more concentrated deep fluid flow in BH-CL37A leading to a shallower SMTZ and more open condition, preventing the accumulation and preservation of authigenic carbonates and barite. Additionally, due to the limited permeability and fluid migration conditions, the locally increased methane leakage at BH-CL37 may not affect BH-CL37A.

5.2.3 cold seep influenced trace elements

The trace elements transported and ultimately enriched in seafloor sediments come from the sinking organic and inorganic particulate matter, as well as the seawater itself (Smrzka et al., 2019). Redox conditions often promote the accumulation of trace elements in sediments due to their redox sensitivity, which leads to the wide application of trace element contents as a proxy of paleo environmental conditions (Tribovillard et al., 2006).

Redox sensitive elements such as U, Mo and other trace elements are often used to trace the redox condition during the formation of cold seep carbonates (Merinero Palomares et al., 2012; Sato et al., 2012; Tribovillard et al., 2012; Hu et al., 2015). In oxidizing seawater, U and Mo are stable and persist for a long time (residence time of U and Mo is 450 kyr and 780 kyr, respectively), but U and Mo behave differently between the anoxic and euxinic

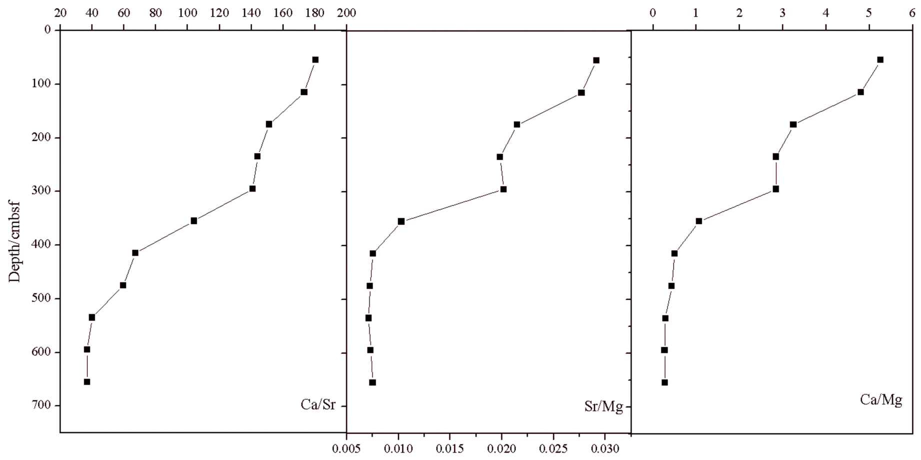

FIGURE 14
Sr/Ca vs Mg/Ca in the sediments. The values of aragonite, biological calcite, calcite and detrital fraction are derived from Yang et al.(2014).

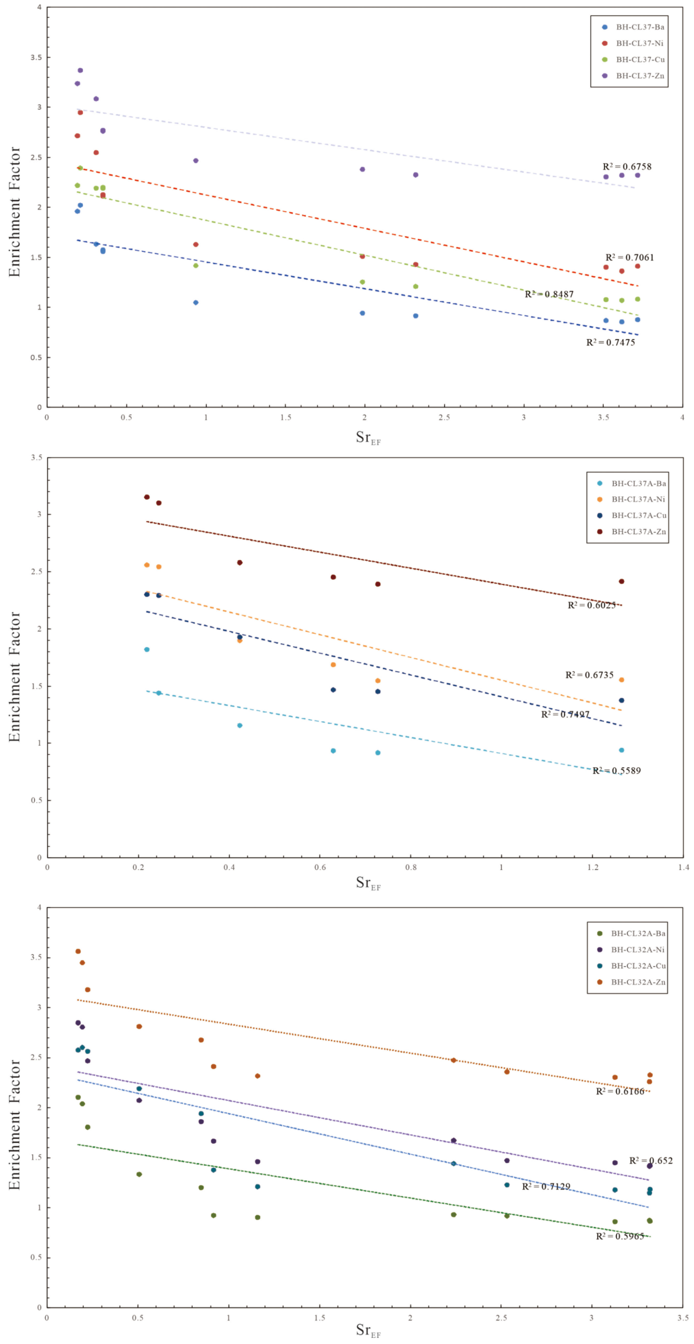

FIGURE 15
Correlations between Sr_{EF} and enrichment factors of trace elements (Ba, Ni, Cu, Zn).

environment (Algeo and Tribovillard, 2009). U exists stably in the soluble form of $UO_2(CO_3)_3^{4-}$ in oxidizing seawater; but in the iron reduction zone, the reduction of iron produces hydrogen sulfide, and U begins to form UO_2 precipitates or be absorbed by organometallic ligands and preserved in sediments (Tribovillard et al., 2006; Smrzka et al., 2019). As a result, U enrichment is stronger than Mo, resulting in the smaller $(Mo/U)_{EF}$ ratio in carbonates than the corresponding ratio in seawater (Algeo and Tribovillard, 2009). Mo mainly exists in the form of MoO_4^{2-}in oxidizing seawater, while in the euxinic environment caused by hydrogen sulfide supersaturation, Mo will transform and combine with metal ions to form a series of Molybdate thiomolybate ($MoS_{4-x}O_x^{2-}$) which is easily captured by iron sulfide or sulfur-rich organic compounds and stored in carbonates, finally resulting in the larger $(Mo/U)_{EF}$ ratio (Algeo and Tribovillard, 2009; Li et al., 2016; Smrzka et al., 2020). Therefore, the different authigenic enrichment degree of U and Mo, and $(Mo/U)_{EF}$ can help to distinguish euxinic condition from anoxic condition effectively.

U tends to enrich in the Fe-Mn reduction zone, while Mo is enriched in sulfate reduction zone (Smrzka et al., 2019; Smrzka et al.,

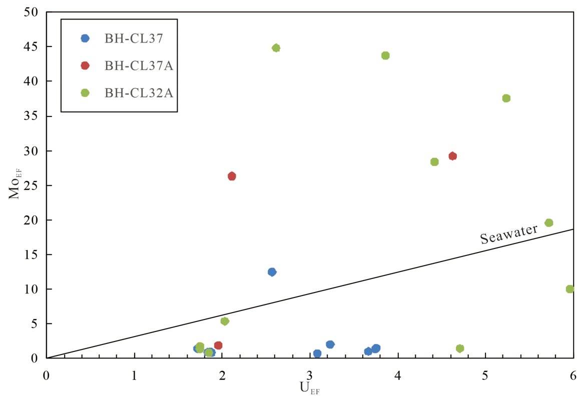

FIGURE 16
Mo_{EF} vs U_{EF}. $(Mo/U)_{EF}$ =3.1 of seawater (Algeo and Tribovillard, 2009).

2020). As shown in Figure 8, U is enriched in the shallow part of the sediments, and the enrichment depth of U varies among different sediment cores. The deeper SMTZ corresponds to the deeper Fe-Mn reduction zone. The Fe-Mn reduction zone of BH-CL37A appears narrower and shallower than that of BH-CL37 due to the stronger methane seepage found in BH-CL37A. Furthermore, the enrichment factors of U in the shallow depths of BH-CL37A are much higher than those of BH-CL37. Studies have shown that the behaviour of U varies greatly with oxygen content and it can be re-mobilized in case of post-deposition reoxygenation (Smrzka et al., 2019; Smrzka et al., 2020). BH-CL37A gains a greater cold seep effect due to the closer distance to the diapir than BH-CL37. The actively upward migration of anoxic fluid prevents the oxic seawater from diffusing into the sediments, so BH-CL37A could better preserve the enrichment of U, while seawater could diffuse downward to deeper formation in BH-CL37, harmful for the preservation of U enrichment. Moreover, considering the obvious change of methane flux in BH-CL37 in the past (discussed in section 5.2.2), the previously formed U precipitate was reactivated and dissolved in pore water due to the reoxygenation, weakening the indicator function of U enrichment. In contrast to BH-CL37, BH-CL37A has enough methane flux to maintain U enrichment even if the methane flux decreases, and the decrease of methane flux would also result in a more focused fluid seepage, protecting the original condition from fast change to some extent. Compared with the enrichment of U, the difference of V enrichment between BH-CL37 and BH-CL37A is not manifest (Figure 8), which further stresses that the decrease of cold seep fluid flow or the decrease after the sudden increase of methane flux does affect the enrichment degree of U by changing the redox conditions of sediments.

In anoxic marine sediments, Mo tends to be incorporated into pyrite by adsorbing molybdate and thiomolybdate to form stable complexes, which can be retained irreversibly (Bostick et al., 2003). Based on our Mo results, we believe that the euxinic environment in the study area is limited to pore water and does not include overlying seawater. Previous studies have shown that in areas where sulfide and thiomolybdate are present but confined to in pore water, Mo content in sediments averages 10 mg/kg and rarely exceeds 25 mg/kg, while Mo content under euxinic condition with free H_2S exceeds 60 mg/kg and can even reach 100 mg/kg in sediments (Scott and Lyons, 2012; Chen et al., 2016). Mo in our study area is significantly enriched at some depths, exceeding 30 μg/g (BH-CL37A: 50-120 cmbsf; BH-CL32A: 230-420 cmbsf) with low Mn contents, indicating euxinic environment in the pore water. OSR and AOM are two main important biochemical reactions related to the sulfate reduction that influence greatly on Mo. However, the low content of organic matter in sediments in the study area and the insignificant enrichment of redox sensitive elements such as Co, Cu, Ni, Zn and V (their enrichment factor are mostly under 3) indicate that OSR is not the main reason for the enrichment of Mo. In fact, rapid AOM reaction will create a suitable euxinic environment for Mo enrichment as a dominant process in cold seeps. It can be concluded from Figure 16 that Mo enrichment factor is greater than U enrichment factor at 350-360 cmbsf of BH-CL37, 50-120 cmbsf of BH-CL37A and 230-420 cmbsf of BH-CL32A, indicating the intense sulfate reduction. Though having the close locations and similar fluid sources, the depth profiles of Mo_{EF} vary greatly: Mo enrichment occurs only at 410-420 cmbsf in BH-CL37, while Mo is enriched significantly in shallow sediments in a wide depth range in BH-CL37A. From the difference of the methane seepage, we deduce that Mo enrichment is more likely to occur in shallow sediments with high methane flux. In methane fluid flow events or high methane flux, methane is transported to the water-sediment interface, and compresses the SMTZ into a narrow area of the topmost sediment cores where sulfate flux and hydrogen sulfide produced by rapid AOM are relatively high. However, deeper SMTZ usually appears with limited Mo availability in BH-CL37 (Figure 17). Comparing the depth profiles of U_{EF} and Mo_{EF}, high methane flux and active cold seep activity tend to compress the Fe-Mn reduction zone and sulfate reduction zone into a narrow area, so Mo and U are enriched within the same depth range (for example, in BH-CL37A, Figure 8). However, under the influence of low methane flux, the sediment core presents a wider sulfate reduction zone and a deeper SMTZ, accompanied by a lower Mo precipitation effect, such as BH-CL37.

BH-CL32A has a deep SMTZ similar as BH-CL37A and the overlap degree of Fe-Mn redox zone and sulfate reduction zone is lower than that of BH-CL37A (the area with high methane flux and high AOM reaction rate). In contrast to BH-CL37, evident Mo enrichment is present in several depth intervals of the shallow sediments here indicating the high AOM reaction rate and the relatively closed structural conditions at certain depths, indicating the high AOM reaction rate and the condition in favor of Mo diffusion.

Previous studies have shown that Mo-Fe-S can co-precipitate from pore water with the threshold of 0.1 μm H_2S, while Mo can co-precipitate with S or precipitate in granular form when H_2S is greater than 100 μm (Zheng et al., 2000; Chen et al., 2016). In other words, Mo can precipitate under the condition of 0.1 μm H_2S content in pore water with sufficient Fe, so the enrichment depth of Mo precipitation in pore water may not be consistent with the depth of H_2S maximum or SMTZ, which contributes to the inconsistent depth of the Mo enrichment and SMTZ in this study.

Other redox sensitive elements, such as Co, Cr, Cu, Zn, V, etc., generally show a relatively consistent trend of enrichment factors,

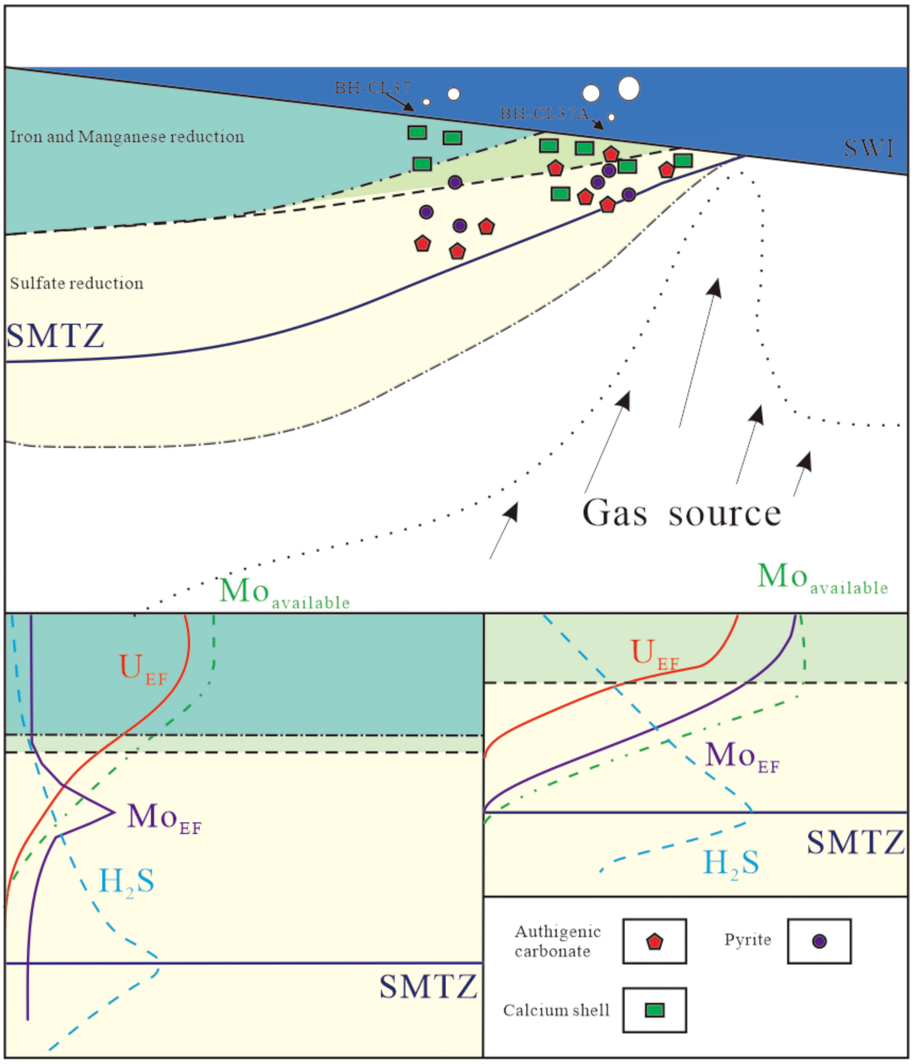

FIGURE 17
Response of different cold seep activities in BH-CL37 and BH-CL37A to geochemistry.

decreasing first and then stabilizing with the increase of depth (Figure 8). According to the Mn/Al image (Figure 7), the higher contents of trace elements in the shallow layer may be mainly from the reductive dissolution of manganese oxides or hydroxides (Tribovillard et al., 2006). Although these trace elements do not show significant enrichment factors, their changes to some extent reflect the changes of redox conditions in the sedimentary environment, and the speed of trace element removals often corresponds to the transition and transformation of iron reduction zone and sulfate reduction zone. As shown in Figure 8, compared with trace elements of BH-CL37, BH-CL37A has a shallower turning depth and a larger gradient of descent, indicating that the intense cold seep activity and large methane flux make the Fe-Mn reduction zone and sulfate reduction zone much closer, narrower and shallower. The enrichment of these trace elements in the shallow sediments reflects the relatively reductive pore water environment under the influence of cold seeps effectively.

The REE+Y distribution curves standardized by PAAS for each sediments cores show similar MREE-enriched pattern (Figure 9). MREE enrichment generally occurs in iron reduction zone and is related to anoxic pore water, indicating the anoxic sedimentary environment. The enrichment of Y shows the obvious influence of seawater. In this study, the samples generally show no Eu anomaly, and most of the samples show no Ce anomaly, while minor shows negative Ce anomaly caused by La anomaly (Figure 10), confirming the reductive condition.

5.3 Evolution and regional specificity of cold seep activity under the influence of different methane fluxes

BH-CL37 and BH-CL37A are two sites impacted by cold seeps located on the same side of the same fluid source with different distances (Figure 2). BH-CL37A closer to the fluid source, is affected by stronger cold seep activity than BH-CL37, and has a larger methane fluid flux. Its intense AOM reaction and the relatively open environment of the shallow SMTZ may make the sulfur isotopes of pyrites in the shallow sediments larger than that of BH-CL37A at the corresponding depth, but less than that of BH-CL37 at deeper down to the bottom. Near the present SMTZ of BH-CL37, the more closed sedimentation environment is conductive to the deposits of authigenic pyrite with higher S isotopic values (>0), but impeding the Mo enrichment (Figure 17).

The seismic profile of BH-CL37 and BH-CL37A shows weak continuity of BSR and the seafloor dome (Figure 2). The low-frequency fuzzy reflection of the underlying layer on one side of the updip of the BSR may indicate the phenomenon of acoustic turbidity caused by gas in the formation and the rich source of methane in the study area, leading to the low background value of $\delta^{13}C_{DIC}$. The obvious geochemical differences between BH-CL37 and BH-CL37A in similar locations may denote the poor seepage conditions, such as low porosity or blocking effect on migration channels due to the formation of gas hydrate. Previous studies have measured that the geothermal gradient in this area is 69.8 °C/km, lower than the average geothermal gradient value of 84.5 °C/km in the Beikang Basin. Strong fluid activity is supposed to cause the change of the thermal field (Milkov, 2000; Feseker et al., 2009; Yang et al., 2018). The lower geothermal gradient indicates the more dispersed fluid diffusion, which corresponds to the wide and deep SMTZ in BH-CL37 and the smaller $\delta^{13}C_{TIC}$ fluctuation gradient (Figure 18). Meanwhile, the abnormally high ion concentrations (Cl^-, Mg^{2+},Ca^{2+}, SO_4^{2-}) in the 50-60 cmbsf of BH-CL37 are interpreted as the abnormal fluid input with high salinity, which may reflect the influence of high-salt fluid caused by the formation of natural gas hydrate, combined with previous studies and its regionally geological structures (Feng J. et al., 2018; Huang et al., 2022).

BH-CL32A has discontinuous BSR and significant submarine gas leakage (Figure 2). Figure 2B shows that BH-CL32A has a relatively isolated fluid migration channel that communicates with the deep strata and extends directly to the seafloor. Combined with its geothermal gradient as high as 102 °C/km, BH-CL32A shows obvious concentrated cold seep fluid upwelling, which is consistent with its high gradient of $\delta^{13}C_{DIC}$ with the narrow area of strong negative values(Figures 5, 18). The compositions of headspace gas in the study area further demonstrate a typical bio-methane source for BH-CL37 and mixed methane source with a significant contribution of the thermogenic gas for BH-CL32A (Huang et al., 2022), which is corresponding to our analysis of the geochemistry of pore water. BH-CL37 and BH-CL32A have similar SMTZ depths, but BH-CL37 has wider depth range of $\delta^{13}C$ strongly deficient (compared with the stable values at the top and bottom of the sediment cores). In general, the background $\delta^{13}C_{DIC}$ values (the average $\delta^{13}C_{DIC}$ of the top and bottom sediments that show stable values of $\delta^{13}C_{DIC}$) of BH-CL32A is slightly higher than that of the other sediment cores. The lower $\delta^{13}C_{DIC}$ values in BH-CL37 and BH-CL37A result from the abundant biogenic methane sources, and the higher values in BH-CL32A confirm the great influence of the thermogenous methane sources. Furthermore, the variation range of $\delta^{13}C_{DIC}$ in SMTZ is comparable to that of BH-CL37A, indicating the intense AOM in SMTZ in BH-CL32A. In BH-CL37, the lower reaction rate of AOM and the lower $\delta^{13}C_{DIC}$ here lead to a wider sulfate reduction zone, so the slope of $\delta^{13}C_{DIC}$ change is less obvious. Besides, BH-CL37 shows a shallower Fe and Mn reduction zone restricted by U enrichment and the lower AOM rate had a limited effect on Mo accumulation. By contrast, the intense and concentrated upwelling of cold seep fluid shown in BH-CL32A activates the exchange of elements between the overlying water and sediments, which is conducive to Mo enrichment.

6 Conclusion

In this paper, we combined geochemical analyses of various samples (pore water, sediments and authigenic pyrites) and the local geological structure to systematically study the cold seep phenomenon in southern SCS on the basis of previous studies. We conclude that SMTZ depth is relatively shallow compared with Feng's study.

The extremely negative $\delta^{13}C_{DIC}$ in the pore water of the sediment cores indicates strong AOM effect in cold seeps and the main biogenic origin of methane. The SO_4^{2-} depth variation trends of pore water, the high DIC content and the lowest value of $\delta^{13}C_{DIC}$ can define the approximate SMTZ depth of each sediment core effectively. In addition, paleo SMTZ depth of about 290-300 cmbsf in BH-CL37 indicates the decrease of methane flux or the sudden release of methane flux in the past.

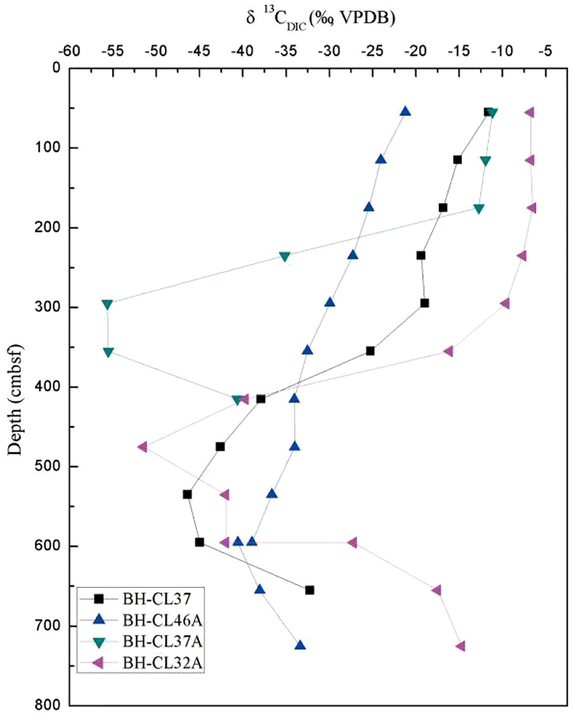

FIGURE 18
Comparison of $\delta^{13}C_{DIC}$ with depth in different sediment cores.

The strong AOM in cold seep leads to the formation of authigenic minerals (authigenic carbonates and authigenic pyrites), and affects the enrichment of trace elements, especially the redox sensitive elements.

BH-CL32A is different from BH-CL37 and BH-CL37A in fluid sources and regional geological structures. The $\delta^{13}C_{DIC}$ value of the background methane in BH-CL32A is higher, which may indicate a greater contribution of thermogenic gas. Furthermore, due to its high AOM rate, BH-CL32A shows a large and steep variation of $\delta^{13}C_{DIC}$ value in pore water, which indicates that the geochemistry in cold seep is closely related to fluid flux, methane sources and local geologic structures.

In conclusion, geologic tectonic conditions such as fluid migration channels in the study area can effectively constrain the generation and evolution of cold seeps, emphasizing the obvious regional specificity of cold seep.

Though many studies on columns and drill cores have been carried out in SCS, the complexity of geological features in the SCS aggravates differences of cold seeps. More quantities of researches on cold seeps in the SCS are inevitably requested for better understanding of cold seeps. With the Sunda continental shelf, one of the most extensive continental shelves in the world, southern SCS has great sensitivity to environmental changes and uniqueness different from northern SCS, pointing to the necessity of researches on cold seep here. Thus, we hope that this study can lay a foundation for the construction of a larger cold seep database in southern SCS and better knowledge of the cold seep system in the future.

Data availability statement

The original contributions presented in the study are publicly available. This data can be found here: https://data.mendeley.com/datasets/d7f9vt5bnt/1.

Author contributions

CC: Writing—original draft, Methodology, Data analysis. XW: Writing—original draft, Data analysis. ZW: Main idea, Methodology, Writing—review and editing. JS: Methodology, Project administration. WH: Methodology, Data analysis. WZha: Data analysis. JL: Supervision. ZX: Data analysis. WZho: Writing—review and editing. LZ: Methodology. All authors contributed to the article and approved the submitted version.

Funding

This work was supported by the Fund of National Nature Science Foundation of China (No. 4207605, 441776056), Innovation Group Project of Southern Marine Science and Engineering Guangdong Laboratory (Zhuhai) (No.311020003/311021004).

Conflict of interest

The authors declare that the research was conducted in the absence of any commercial or financial relationships that could be construed as a potential conflict of interest.

Publisher's note

References

Algeo, T. J., and Tribovillard, N. (2009). Environmental analysis of paleoceanographic systems based on molybdenum-uranium covariation. *Chem. Geol.* 268, 211–225. doi: 10.1016/j.chemgeo.2009.09.001

Bau, M., and Dulski, P. (1996). Distribution of yttrium and rare-earth elements in the penge and kuruman iron-formations, Transvaal supergroup, south Africa. *Precambrian Res.* 79, 37–55. doi: 10.1016/0301-9268(95)00087-9

Bayon, G., Henderson, G. M., Etoubleau, J., Caprais, J.-C., Ruffine, L., Marsset, T., et al. (2015). U-Th Isotope constraints on gas hydrate and pockmark dynamics at the Niger delta margin. *Mar. Geol.* 370, 87–98. doi: 10.1016/j.margeo.2015.10.012

Bayon, G., Pierre, C., Etoubleau, J., Voisset, M., Cauquil, E., Marsset, T., et al. (2007). Sr/Ca and Mg/Ca ratios in Niger delta sediments: Implications for authigenic carbonate genesis in cold seep environments. *Mar. Geol.* 241, 93–109. doi: 10.1016/j.margeo.2007.03.007

Berner, R. (1980). *Early diagenesis: A theoretical approach* (Princeton: Princeton University Press). doi: 10.1515/9780691209401

Boetius, A., Ravenschlag, K., Schubert, C. J., Rickert, D., Widdel, F., Gieseke, A., et al. (2000). A marine microbial consortium apparently mediating anaerobic oxidation of methane. *Nature* 407, 623–626. doi: 10.1038/35036572

Boetius, A., and Wenzhöfer, F. (2013). Seafloor oxygen consumption fuelled by methane from cold seeps. *Nat. Geosci.* 6, 725–734. doi: 10.1038/ngeo1926

Borowski, W., Hoehler, T., Alperin, M., Rodriguez, N., and Paull, C. (2000). 9. significance of anaerobic methane oxidation in methane-rich sediments overlying the Blake ridge gas hydrates. *Proc. Ocean Drill. Progr. Sci. Results* 164, 87–99. doi: 10.2973/odp.proc.sr.164.214.2000

Borowski, W. S., Paull, C. K., and Ussler, W. (1996). Marine pore-water sulfate profiles indicate *in situ* methane flux from underlying gas hydrate. *Geology* 24, 655–658. doi: 10.1130/0091-7613(1996)024<0655:MPWSPI>2.3.CO;2

Borowski, W. S., Paull, C. K., and Ussler, W.III (1999). Global and local variations of interstitial sulfate gradients in deep-water, continental margin sediments: Sensitivity to underlying methane and gas hydrates. *Mar. Geol.* 159, 131–154. doi: 10.1016/S0025-3227(99)00004-3

Borowski, W. S., Rodriguez, N. M., Paull, C. K., and Ussler, W. (2013). Are 34S-enriched authigenic sulfide minerals a proxy for elevated methane flux and gas hydrates in the geologic record? *Mar. Pet. Geol.* 43, 381–395. doi: 10.1016/j.marpetgeo.2012.12.009

Bostick, B. C., Fendorf, S., and Helz, G. R. (2003). Differential adsorption of molybdate and tetrathiomolybdate on pyrite (FeS2). *Environ. Sci. Technol.* 37, 285–291. doi: 10.1021/es0257467

Boudreau, B. P. (1997). "Diagenetic models and their implementation: modeling transport and reactions in aquatic sediments," *Diagenetic Models and Their Implementation*, vol. 414. (New York: Springer).

Campbell, K. A. (2006). Hydrocarbon seep and hydrothermal vent paleoenvironments and paleontology: Past developments and future research directions. *Palaeogeogr. Palaeoclimatol. Palaeoecol.* 232, 362–407. doi: 10.1016/j.palaeo.2005.06.018

Canfield, D. E., and Thamdrup, B. (1994). The production of 34S-depleted sulfide during bacterial disproportionation of elemental sulfur. *Science* 266, 1973–1975. doi: 10.1126/science.11540246

Castellini, D. G., Dickens, G. R., Snyder, G. T., and Ruppel, C. D. (2006). Barium cycling in shallow sediment above active mud volcanoes in the gulf of Mexico. *Chem. Geol.* 226, 1–30. doi: 10.1016/j.chemgeo.2005.08.008

Chen, F., Hu, Y., Feng, D., Zhang, X., Cheng, S., Cao, J., et al. (2016). Evidence of intense methane seepages from molybdenum enrichments in gas hydrate-bearing sediments of the northern south China Sea. *Chem. Geol.* 443, 173–181. doi: 10.1016/j.chemgeo.2016.09.029

Chen, A., Xu, H., Luo, X., Liao, K., and Peng, D. (2017). Heat flow characteristics and controlling factors of the Baikang Basin in South China sea. *Acta Geologica Sinica* 91 (08):1720–1728. doi: 10.1007/s11430-010-0018-y

Chen, Z., Huang, C.-Y., Wu, B., and Yan, W. (2010). Discovery of native aluminum and its possible origin from prospective gas hydrate areas in the south China Sea. *Sci. China Earth Sci.* 53, 335–344. doi: 10.1007/s11430-010-0018-y

Chen, Y., Ussler, W., Haflidason, H., Lepland, A., Rise, L., Hovland, M., et al. (2010). Sources of methane inferred from pore-water δ13C of dissolved inorganic carbon in pockmark G11, offshore mid-Norway. *Chem. Geol.* 275, 127–138. doi: 10.1016/j.chemgeo.2010.04.013

Chen, Z., Yan, W., Tang, X., Liu, J., Chen, M., and Yang, H. (2009). Magnetic susceptibility in surface sediments in the southern south China Sea and its implication for sub-sea methane venting. *J. Earth Sci.* 20, 193–204. doi: 10.1007/s12583-009-0019-y

Claypool, G., Milkov, A., Lee, Y.-J., Torres, M., Borowski, W., and Tomaru, H. (2006). Microbial methane generation and gas transport in shallow sediments of an accretionary complex, southern hydrate ridge (ODP leg 204), offshore Oregon, USA. *Proc. Ocean Drill. Progr. Sci. Results* 204, 1–52. doi: 10.2973/odp.proc.sr.204.113.2006

Crémière, A., Lepland, A., Chand, S., Sahy, D., Kirsimäe, K., Bau, M., et al. (2016). Fluid source and methane-related diagenetic processes recorded in cold seep carbonates from the alvheim channel, central north Sea. *Chem. Geol.* 432, 16–33. doi: 10.1016/j.chemgeo.2016.03.019

Dickens, G. R. (2001). Sulfate profiles and barium fronts in sediment on the Blake ridge: present and past methane fluxes through a large gas hydrate reservoir. *Geochim. Cosmochim. Acta* 65, 529–543. doi: 10.1016/S0016-7037(00)00556-1

Feng, D., and Chen, D. (2015). Authigenic carbonates from an active cold seep of the northern south China Sea: New insights into fluid sources and past seepage activity. *Deep Sea Res. Part II Top. Stud. Oceanogr.* 122, 74–83. doi: 10.1016/j.dsr2.2015.02.003

Feng, D., Qiu, J. W., Hu, Y., Peckmann, J., Guan, H., Tong, H., et al. (2018). Cold seep systems in the south China Sea: An overview. *J. Asian Earth Sci.* 168, 3–16. doi: 10.1016/j.jseaes.2018.09.021

Feng, J., Yang, S., Liang, J., Fang, Y., He, Y., Luo, M., et al. (2018). Methane seepage inferred from the porewater geochemistry of shallow sediments in the beikang basin of the southern south China Sea. *J. Asian Earth Sci.* 168, 77–86. doi: 10.1016/j.jseaes.2018.02.005

Feseker, T., Dählmann, A., Foucher, J.-P., and Harmegnies, F. (2009). *In-situ* sediment temperature measurements and geochemical porewater data suggest highly dynamic fluid flow at Isis mud volcano, eastern Mediterranean Sea. *Mar. Geol.* 261, 128–137. doi: 10.1016/j.margeo.2008.09.003

Fu, S. (2007). Study on paleoclimate and paleoenvironment in the SouthernSouth China Sea since the late quaternary. *Diss. GSCAS.*

Gibson, R., Atkinson, R., Gordon, J., Editors, T., In, F., and Carney, R. (2005). Zonation of deep biota on continental margins. *Annu. Rev.* 43, 211–278. doi: 10.1201/9781420037449-8

Gong, S., Hu, Y., Li, N., Feng, D., Liang, Q., Tong, H., et al. (2018). Environmental controls on sulfur isotopic compositions of sulfide minerals in seep carbonates from the south China Sea. *J. Asian Earth Sci.* 168, 96–105. doi: 10.1016/j.jseaes.2018.04.037

Hu, Y., Feng, D., Liang, Q., Xia, Z., Chen, L., and Chen, D. (2015). Impact of anaerobic oxidation of methane on the geochemical cycle of redox-sensitive elements at cold-seep sites of the northern south China Sea. *Deep. Res. Part II Top. Stud. Oceanogr.* 122, 84–94. doi: 10.1016/j.dsr2.2015.06.012

Hu, Y., Luo, M., Chen, L., Liang, Q., Feng, D., Tao, J., et al. (2018). Methane source linked to gas hydrate system at hydrate drilling areas of the south China Sea: Porewater geochemistry and numerical model constraints. *J. Asian Earth Sci.* 168, 87–95. doi: 10.1016/j.jseaes.2018.04.028

Huang, W., Meng, M., Zhang, W., Shang, J., Liang, J., and Wan, Z. (2022). Geological, geophysical, and geochemical characteristics of deep-routed fluid seepage and its indication of gas hydrate occurrence in the beikang basin, southern south China Sea. *Mar. Pet. Geol.* 139, 105610. doi: 10.1016/j.marpetgeo.2022.105610

Ingram, W. C., Meyers, S. R., Shen, Z., Xu, H., and Martens, C. S. (2016). Manganese enrichments near a large gas-hydrate and cold-seep field: a record of past redox and sedimentation events. *Depos. Rec.* 2, 142–153. doi: 10.1002/dep2.18

Jørgensen, B. B., Böttcher, M. E., Lüschen, H., Neretin, L. N., and Volkov, I. I. (2004). Anaerobic methane oxidation and a deep H2S sink generate isotopically heavy sulfides in black Sea sediments. *Geochim. Cosmochim. Acta* 68, 2095–2118. doi: 10.1016/j.gca.2003.07.017

Joseph, C., Campbell, K. A., Torres, M. E., Martin, R. A., Pohlman, J. W., Riedel, M., et al. (2013). Methane-derived authigenic carbonates from modern and paleoseeps on the cascadia margin: Mechanisms of formation and diagenetic signals. *Palaeogeogr. Palaeoclimatol. Palaeoecol.* 390, 52–67. doi: 10.1016/j.palaeo.2013.01.012

Karaca, D., Hensen, C., and Wallmann, K. (2010). Controls on authigenic carbonate precipitation at cold seeps along the convergent margin off Costa Rica. *Geochem. Geophys. Geosyst* 11, Q08S27. doi: 10.1029/2010GC003062

Kim, J.-H., Park, M.-H., and Chun, J.-H. (2011). Molecular and isotopic signatures in sediments and gas hydrate of the central/southwestern ulleung basin: high alkalinity escape fuelled by biogenically sourced methane. *Geo-Mar Lett* 31:37–49. doi: 10.1007/s00367-010-0214-y

Levin, L. A. (2005). Ecology of cold seep sediments: Interactions of fauna with flow, chemistry and microbes. *Oceanogr. Mar. Biol.* 43, 1–46. doi: 10.1201/9781420037449.ch1

Levin, L. A., and Sibuet, M. (2012). Understanding continental margin biodiversity: A new imperative. *Ann. Rev. Mar. Sci.* 4, 79–112. doi: 10.1146/annurev-marine-120709-142714

Li, N., Feng, D., Chen, L., Wang, H., and Chen, D. (2016). Using sediment geochemistry to infer temporal variation of methane flux at a cold seep in the south China Sea. *Mar. Pet. Geol.* 77, 835–845. doi: 10.1016/j.marpetgeo.2016.07.026

Li, N., Yang, X., Peng, J., Zhou, Q., and Chen, D. (2018). Paleo-cold seep activity in the southern south China Sea: Evidence from the geochemical and geophysical records of sediments. *J. Asian Earth Sci.* 168, 106–111. doi: 10.1016/j.jseaes.2017.10.022

Liang, Q., Hu, Y., Feng, D., Peckmann, J., Chen, L., Yang, S., et al. (2017). Authigenic carbonates from newly discovered active cold seeps on the northwestern slope of the south China Sea: Constraints on fluid sources, formation environments, and seepage dynamics. *Deep. Res. Part I Oceanogr. Res. Pap.* 124, 31–41. doi: 10.1016/j.dsr.2017.04.015

Lin, Z., Sun, X., Peckmann, J., Lu, Y., Xu, L., Strauss, H., et al. (2016). How sulfate-driven anaerobic oxidation of methane affects the sulfur isotopic composition of pyrite: A SIMS study from the south China Sea. *Chem. Geol.* 440, 26–41. doi: 10.1016/j.chemgeo.2016.07.007

Lin, Z., Sun, X., Strauss, H., Lu, Y., Gong, J., Xu, L., et al. (2017). Multiple sulfur isotope constraints on sulfate-driven anaerobic oxidation of methane: Evidence from authigenic pyrite in seepage areas of the south China Sea. *Geochim. Cosmochim. Acta* 211, 153–173. doi: 10.1016/j.gca.2017.05.015

Lin, Q., Wang, J., Algeo, T. J., Sun, F., and Lin, R. (2016). Enhanced framboidal pyrite formation related to anaerobic oxidation of methane in the sulfate-methane transition zone of the northern south China Sea. *Mar. Geol.* 379, 100–108. doi: 10.1016/j.margeo.2016.05.016

Liu, H., Yao, Y., and Deng, H. (2011). Geological and geophysical conditions for potential natural gas hydrate resources in southern south China Sea waters. *J. Earth Sci.* 22, 718–723. doi: 10.1007/s12583-011-0222-5

Luff, R., and Wallmann, K. (2003). Fluid flow, methane fluxes, carbonate precipitation and biogeochemical turnover in gas hydrate-bearing sediments at hydrate ridge, cascadia margin: numerical modeling and mass balances. *Geochim. Cosmochim. Acta* 67, 3403–3421. doi: 10.1016/S0016-7037(03)00127-3

Luff, R., Wallmann, K., and Aloisi, G. (2004). Numerical modeling of carbonate crust formation at cold vent sites: significance for fluid and methane budgets and chemosynthetic biological communities. *Earth Planet. Sci. Lett.* 221, 337–353. doi: 10.1016/S0012-821X(04)00107-4

Malinverno, A., and Pohlman, J. W. (2011). Modeling sulfate reduction in methane hydrate-bearing continental margin sediments: Does a sulfate-methane transition require anaerobic oxidation of methane? *Geochem. Geophys. Geosyst.* 12, Q07006. doi: 10.1029/2011GC003501

McLennan, S. (2001). Relationships between the trace element composition of sedimentary rocks and upper continental crust. geochemistry geophys. *Geosystems - GEOCHEM Geophys GEOSYST* 2. doi: 10.1029/2000GC000109

Merinero Palomares, R., Lunar Hernández, R., and Martínez Frías, J. (2012). Mechanisms of trace metal enrichment in submarine, methane-derived carbonate chimneys from the gulf of cadiz. *J. Geochemical Explor.* 112, 297–305. doi: 10.1016/j.gexplo.2011.09.011

Michaelis, W., Seifert, R., Nauhaus, K., Treude, T., Thiel, V., Blumenberg, M., et al. (2002). Microbial reefs in the black Sea fueled by anaerobic oxidation of methane. *Science* 297, 1013–1015. doi: 10.1126/science.1072502

Milkov, A. V. (2000). Worldwide distribution of submarine mud volcanoes and associated gas hydrates. *Mar. Geol.* 167, 29–42. doi: 10.1016/S0025-3227(00)00022-0

Morley, C. K. (2012). Late Cretaceous–early palaeogene tectonic development of SE Asia. *Earth-Science Rev.* 115, 37–75. doi: 10.1016/j.earscirev.2012.08.002

Orphan, V., Hinrichs, K.-U., Ussler, B., Paull, C., Taylor, L., Sylva, S., et al. (2001). Comparative analysis of methane-oxidizing archaea and sulfate-reducing bacteria in anoxic marine sediments. *Appl. Environ. Microbiol.* 67, 1922–1934. doi: 10.1128/AEM.67.4.1922-1934.2001

Peketi, A., Mazumdar, A., Joao, H. M., Patil, D. J., Usapkar, A., and Dewangan, P. (2015). Coupled c-S-Fe geochemistry in a rapidly accumulating marine sedimentary system: diagenetic and depositional implications. *Geochem. Geophys. Geosyst.* 16, 2865–22883. doi: 10.1002/2015GC005754

Reeburgh, W. (2007). Oceanic methane biogeochemistry. *Chem. Rev.* 107, 486–513. doi: 10.1021/cr050362v

Rees, C. E., Jenkins, W. J., and Monster, J. (1978). The sulphur isotopic composition of ocean water sulphate. *Geochim. Cosmochim. Acta* 42, 377–381. doi: 10.1016/0016-7037(78)90268-5

Riedinger, N., Kasten, S., Gröger, J., Franke, C., and Pfeifer, K. (2006). Active and buried authigenic barite fronts in sediments from the Eastern cape basin. *Earth Planet. Sci. Lett.* 241, 876–887. doi: 10.1016/j.epsl.2005.10.032

Sackett, W. M. (1978). Carbon and hydrogen isotope effects during the thermocatalytic production of hydrocarbons in laboratory simulation experiments. *Geochim. Cosmochim. Acta* 42, 571–580. doi: 10.1016/0016-7037(78)90002-9

Sato, H., Hayashi, K. I., Ogawa, Y., and Kawamura, K. (2012). Geochemistry of deep sea sediments at cold seep sites in the nankai trough: Insights into the effect of anaerobic oxidation of methane. *Mar. Geol.* 323–325, 47–55. doi: 10.1016/j.margeo.2012.07.013

Scott, C., and Lyons, T. W. (2012). Contrasting molybdenum cycling and isotopicproperties in euxinic versus non-euxinic sediments and sedimentary rocks: Refining the paleoproxies. *Chem. Geol.* 324–325, 19–27. doi: 10.1016/j.chemgeo.2012.05.012

Shields, G. A., and Webb, G. E. (2004). Has the REE composition of seawater changed over geological time? *Chem. Geol.* 204, 103–107. doi: 10.1016/j.chemgeo.2003.09.010

Smrzka, D., Feng, D., Himmler, T., Zwicker, J., Hu, Y., Monien, P., et al. (2020). Trace elements in methane-seep carbonates: Potentials, limitations, and perspectives. *Earth-Science Rev.* 208. doi: 10.1016/j.earscirev.2020.103263

Smrzka, D., Zwicker, J., Bach, W., Feng, D., Himmler, T., Chen, D., et al. (2019). *The behavior of trace elements in seawater, sedimentary pore water, and their incorporation into carbonate minerals: a review, facies* (Berlin Heidelberg: Springer). doi: 10.1007/s10347-019-0581-4

Snyder, G. T., Dickens, G. R., and Castellini, D. G. (2007). Labile barite contents and dissolved barium concentrations on Blake ridge: New perspectives on barium cycling above gas hydrate systems. *J. Geochemical Explor.* 95, 48–65. doi: 10.1016/j.gexplo.2007.06.001

Su, X., Chen, F., Yu, X., and Huang, Y. (2005). A pilot study on Miocene through Holocene sediments from the continental slope of the south China Sea in correlation with possible distribution of gas hydrates. *Geoscience* 19, 1–13.

Suess, E. (2014). Marine cold seeps and their manifestations: geological control, biogeochemical criteria and environmental conditions. *Int. J. Earth Sci.* 103, 1889–1916. doi: 10.1007/s00531-014-1010-0

Tong, H., Feng, D., Cheng, H., Yang, S., Wang, H., Min, A. G., et al. (2013). Authigenic carbonates from seeps on the northern continental slope of the south China Sea: New insights into fluid sources and geochronology. *Mar. Pet. Geol.* 43, 260–271. doi: 10.1016/j.marpetgeo.2013.01.011

Torres, M. E., Brumsack, H. J., Bohrmann, G., and Emeis, K. C. (1996). Barite fronts in continental margin sediments: a new look at barium remobilization in the zone of sulfate reduction and formation of heavy barites in diagenetic fronts. *Chem. Geol.* 127, 125–139. doi: 10.1016/0009-2541(95)00090-9

Tribovillard, N., Algeo, T. J., Baudin, F., and Riboulleau, A. (2012). Analysis of marine environmental conditions based onmolybdenum–uranium covariation–applications to mesozoic paleoceanography. *Chem. Geol.* 324–325, 46–58. doi: 10.1016/j.chemgeo.2011.09.009

Tribovillard, N., Algeo, T. J., Lyons, T., and Riboulleau, A. (2006). Trace metals as paleoredox and paleoproductivity proxies: An update. *Chem. Geol.* 232, 12–32. doi: 10.1016/j.chemgeo.2006.02.012

Tribovillard, N., Du Châtelet, E. A., Gay, A., Barbecot, F., Sansjofre, P., and Potdevin, J. L. (2013). Geochemistry of cold seepage-impacted sediments: Per-ascensum or per-descensum trace metal enrichment? *Chem. Geol.* 340, 1–12. doi: 10.1016/j.chemgeo.2012.12.012

Trung, N. N. (2012). The gas hydrate potential in the south China Sea. *J. Pet. Sci. Eng.* 88–89, 41–47. doi: 10.1016/j.petrol.2012.01.007

Vanneste, H., James, R. H., Kelly-Gerreyn, B. A., and Mills, R. A. (2013). Authigenic barite records of methane seepage at the carlos ribeiro mud volcano (Gulf of cadiz). *Chem. Geol.* 354, 42–54. doi: 10.1016/j.chemgeo.2013.06.010

Wan, Z., Chen, C., Liang, J., Zhang, W., Huang, W., and Su, P. (2020). Hydrochemical characteristics and evolution mode of cold seeps in the qiongdongnan basin, south China Sea. *Geofluids.* doi: 10.1155/2020/4578967

Wang, M., Cai, F., Li, Q., Liang, J., Yan, G. J., Dong, G., et al. (2015). Characteristics of authigenic pyrite and its sulfur isotopes, influenced by methane seep at Core A, Site 79 of the middle Okinawa trough. *Sci. China: Earth Sci.* 45, 1819–1828. doi: 10.1007/s11430-015-5196-1

Wang, X., Li, N., Feng, D., Hu, Y., Bayon, G., Liang, Q., et al. (2018). Using chemical compositions of sediments to constrain methane seepage dynamics: A case study from haima cold seeps of the south China Sea. *J. Asian Earth Sci.* 168, 137–144. doi: 10.1016/j.jseaes.2018.11.011

Wang, S., Yan, W., and Song, H. (2006). Mapping the thickness of the gas hydrate stability zone in the south China Sea. *Terr. Atmos. Ocean. Sci.* 17, 815–828. doi: 10.3319/TAO.2006.17.4.815(GH

Wang, S., Yan, W., Song, H., and Fan, S. (2005). Change of gas hydrate reservoirs in the southern south China Sea from the last glacial maximum to present and its effect on the environmen. *Chin. J. Geophys* 48 (5), 1117–1124. doi: 10.1002/cjg2.764

Wang, H., Zhang, G., Yang, M., Liang, J., Liang, J., and Zhong, G. (2003). Structural circumstance of gas hydrate deposition in the continent margin, the south China Sea. *Mar. Geol. Quat. Geol* 23, 82–83. doi: CNKI:SUN:HYDZ.0.2003-01-013

Wei, W., Zhang, J., Wei, X., and Wang, Y. (2012). Resource potential analysis of natural gas hydrate in south China Sea. *Prog. Geophys* 27, 2646–2655. doi: CNKI: SUN: DQWJ.0.2012-06-044

Whiticar, M. J. (1999). Carbon and hydrogen isotope systematics of bacterial formation and oxidation of methane. *Chem. Geol.* 161, 291–314. doi: 10.1016/S0009-2541(99)00092-3

Xie, X., Zhang, C., Ren, J., Yao, B., Wan, L., Chen, H., et al. (2011). Effects of distinct tectonic evolutions on hydrocarbon accumulation in northern and southern continental marginal basins of the south China Sea. *Chin. J. Geophys* 54, 3280–3291. doi: 10.1002/cjg2.1687

Yan, W., Zhang, G., Zhang, L., Xia, B., Yang, Z., Lei, Z., et al. (2018). Focused fluid flow systems and their implications for hydrocarbon accumulations on the southern margin of south China Sea. *Geol. China* 45, 39–47. doi: 10.12029/gc20180104

Yang, K., Chu, F., Ye, L., Zhang, W., Xu, D., Zhu, J., et al. (2014). Implication of methane seeps from sedimentary geochemical proxies (Sr/Ca & Mg/Ca) in the northern south China Sea. *J. Jilin Univ. Earth Sci. Ed.* 44, 469–479. doi: 10.13278/j.cnki.jjuese.201402106

Yang, H.-T., Yang, D.-B., Mu, M.-S., Wang, A.-Q., Quan, Y.-K., Hao, L.-R., et al. (2019). Sr–Nd–Hf isotopic compositions of lamprophyres in western Shandong, China: Implications for the nature of the early cretaceous lithospheric mantle beneath the eastern north China craton. *Lithos.* 336–337, 1–13. doi: 10.1016/j.lithos.2019.03.030

Yang, X., Zhong, S., and Wan, Z. (2018). The thermodynamics of mud diapir/volcano fluidand its influence on gas hydrate occurrence. *Mar. Geology Front.* 34, 15–23. doi: 10.16028/j.1009-2722.2018.07003

Yao, B. (2007). The forming condition and distribution characteristics of the gas hydrate in the south China Sea. *Offshore Oil* 27, 1–10. doi: CNKI:SUN:HYDZ.0.2005-02-017

Zhang, G., Zhu, W., Mi, L., Zhang, H., Liang, J., and Qu, H. (2010). The theory of hydrocarbon generation controlled by source rock and heat from circle distribution of outside-oil fields and inside-gas fields in south China Sea. *Acta Sedimentol. Sin.* 28, 987–1005. doi: 10.1017/S0004972710001772

Zheng, Y., Anderson, R. F., Van Geen, A., and Kuwabara, J. (2000). Authigenic molybdenum formation in marine sediments: a link to pore water sulfide in the Santa Barbara basin. *Geochim. Cosmochim. Acta* 64, 4165–4178. doi: 10.1016/S0016-7037(00)00495-6

Zhu, Y., Zhang, G., and Lou, Z. (2001). Gas hydrate in the south China Sea: background and indicators. *Acta Petrol. Sin.* 22, 6–10. doi: 10.3321/j.issn:0253-2697.2001.05.002